1 Dispersive Fluxes within and over a Real Urban Canopy: A

2 Large-Eddy Simulation Study

3 Emmanuel Akinlabi¹ • Björn Maronga² • Marco G. Giometto³ • Dan Li¹

- 4 Received: DD Month YEAR/ Accepted: DD Month YEAR/ Published online: DD Month YEAR
- 5 © Springer Science + Business Media B. V.

6 Abstract

- 7 Large eddy simulations (LES) are conducted to study the transport of momentum and
- 8 passive scalar within and over a real urban canopy in the City of Boston, United States.
- 9 This urban canopy is characterized by complex building layouts, densities and orientations
- with high-rise buildings. Special attention is given to the magnitude, variability, and
- 11 structure of dispersive momentum and scalar fluxes and their relative importance to
- turbulent momentum and scalar fluxes. We first evaluate the LES model by comparing the
- simulated flow statistics over an urban-like canopy to data reported in previous studies. In
- simulations over the considered real urban canopy, we observe that the dispersive
- momentum and scalar fluxes can be important beyond 2-5 times the mean building height,
- which is a commonly used definition for the urban roughness sublayer height. Above the
- mean building height where the dispersive fluxes become weakly dependent on the grid
- spacing, the dispersive momentum flux contributes about 10% 15% to the sum of
- 19 turbulent and dispersive momentum fluxes and does not decrease monotonically with
- 20 increasing height. The dispersive momentum and scalar fluxes are sensitive to the time and
- 21 spatial averaging. We further find that the constituents of dispersive fluxes are spatially
- heterogeneous and enhanced by the presence of high-rise buildings. This work suggests the
- 23 need to parameterize both turbulent and dispersive fluxes over real urban canopies in
- 24 mesoscale and large-scale models.

Emmanuel Akinlabi akinlabi@bu.edu

Department of Earth and Environment, Boston University, MA, 02215, USA

² Institute of Meteorology and Climatology, Leibniz Universität Hannover, Hannover, Germany

Department of Civil Engineering and Engineering Mechanics, Columbia University in the City of New York, 500 W 120th St, New York, NY 10027, USA

- **Keywords** Dispersive fluxes Large-eddy simulation Real urban canopy Urban
- 26 roughness sublayer

1 Introduction

The world's urban population has seen unprecedented growth over the last decade and 68% of people are expected to live in cities by 2050 (United Nations 2018). As a result, urban systems have received significant attention in many fields, including meteorology. Studies on urban weather and air quality forecasting, the dispersion of air pollutants, and the impact of new construction projects on urban climate are urgently needed to develop sustainable and resilient cities and improve the quality of life of urban dwellers (Britter et al. 2003; Fernando et al. 2001, 2010; Barlow et al. 2017). Advancing the current understanding and modeling capabilities of momentum and scalar transport in the so-called urban roughness sublayer (RSL) is critical to address these issues. The urban RSL is the lowest part of the urban atmospheric boundary layer, where the atmospheric flow is directly affected by the presence of roughness elements (such as buildings, trees, cars etc.). Flow and transport in the urban RSL are complex and highly heterogeneous precisely due to the interactions between the turbulence and the varying arrangement and morphology of the roughness elements (Wang et al. 2014; Auvinen et al. 2020; Cheng et al. 2021; Torres et al. 2021). A commonly used definition for the urban RSL height is about 2-5 times the mean building height (Oke et al. 2017).

Most urban parameterizations represent the complexities of urban RSL via one-dimensional approaches. One-dimensional approaches such as Monin-Obukhov similarity theory (Monin and Obukhov 1954; Obukhov 1971) relying on horizontal homogeneity have been shown to be inapplicable in the urban RSL (Rotach 1999; Roth 2000). Hence, better models that account for the inherently complex urban topology are strongly needed (Britter and Hanna 2003). By averaging the conservation equations over time and space, often called the double-averaging procedure (Xie and Fuka 2018; Schmid et al. 2019), terms that result from spatial heterogeneities in the time-averaged flow need to be considered (Mahrt 1987; Mahrt 2010). These terms have different names in different fields. For example, in canopy studies, they are called dispersive fluxes (Raupach and Shaw 1982) while in the global atmospheric modeling literature, they are often called mesoscale fluxes

(Avissar and Chen 1993; Chen and Avissar 1994). In studies of land surface heterogeneity, similar terms have been called heterogeneity-induced fluxes (Maronga and Raasch 2013; Zhou et al. 2018). But these fluxes all represent the spatial variabilities in the time-averaged flow fields within a certain domain (or over a certain scale) or unresolved, time-lasting advection fluxes generated by a-priori unresolved spatial heterogeneities (Calaf et al. 2020). Throughout this paper, they will be called dispersive fluxes. These dispersive fluxes, especially the dispersive scalar fluxes, remain poorly understood, which motivates this study.

55

56

57

58

59

60

61

62

63

64

65

66

67

68

69

70

71

72

73

74

75

76

77

78

79

80

81

82

83

84

85

The study of dispersive fluxes originates from vegetation canopies (Finnigan 2000; Raupach and Shaw 1982) and gradually moves to other types of canopies. However, their relative importance to turbulent fluxes remains debated and whether they need to be parameterized in large-scale models is unclear. Using wind tunnel measurements, studies showed that the dispersive momentum fluxes are negligible throughout the depth of densely placed plant or urban-like canopy (Raupach et al. 1986; Raupach 1994; Kaimal and Finnigan 1994; Cheng and Castro 2002). In contrast, other investigations have shown that dispersive fluxes play an important role in the description of spatially averaged flow statistics (Bohm et al. 2000; Poggi et al. 2004; Martilli and Santiago 2007; Niroobakhsh et al. 2022). For example, Mignot et al. (2009) found that dispersive fluxes were about 6% of the total fluxes in gravel bed channel flows. However, Bailey and Stoll (2013) showed that the dispersive momentum flux was more than 20% of the turbulent momentum flux in sparse, vegetative canopies. In urban canopy studies, due to the complex pressure field and velocity variations, the dispersive fluxes are formed around canopy edges, and they can be large in the entry region and at the canopy top (Moltchanov et al. 2015). Li and Bou-Zeid (2019) confirmed the significance of dispersive fluxes over urban canopies and studied the effect of changing urban geometry on dispersive fluxes. They showed that the dispersive momentum flux can be about 50% of the total flux, especially for the most eccentric urban geometry. Studies of flow over real urban canopies also confirm the importance of dispersive momentum fluxes (Giometto et al. 2016; Cheng et al. 2021) but little is known about the dispersive scalar flux. Thus, it may be summarized that the importance of dispersive fluxes is highly dependent on a range of morphological factors, including but not limited to canopy densities and heights (Kanda et al. 2013; Sützl et al. 2021). Moreover,

the sensitivities of dispersive fluxes to time/spatial averaging scales and grid resolution remain poorly understood, especially over real canopies. For example, previous studies emphasized that a much longer averaging time is needed to compute dispersive fluxes compared to the computation of turbulent fluxes due to the presence of slowly evolving mean circulations (Coceal et al. 2006; Leonardi et al. 2010, 2015). However, it is still unknown how the dispersive fluxes over real urban canopies depend on the averaging time and spatial scales.

Research on dispersive fluxes in urban RSL has been often carried out over simplified urban-like configurations, mostly in the form of staggered/aligned cube-, cuboid- or rodlike obstacles (Cheng and Castro 2002; Rasheed and Robinson 2013; Leonardi et al. 2015; Blunn et al. 2022; Sützl et al. 2021). These studies examined the dispersive fluxes under various geometric factors such as aspect ratios, orientations and packing densities (Coceal et al. 2006; Cheng et al. 2007; Bou-Zeid et. al. 2009; Herpin et al. 2018; Li and Bou-Zeid 2019). These studies were justified on the grounds that it is better to understand flows over simple configurations before introducing other forms of complexities such as variable roughness heights, orientations, and/or shapes (Sützl et. al. 2021). However, flows over urban-like canopies are different from those over real urban canopies because of the intrinsic surface heterogeneity and the varied aerodynamic properties of individual roughness elements in the real world (Kanda et al. 2013; Giometto et al. 2016; Auvinen et al. 2020). Moreover, the increase in urban population necessitates the construction of highrise buildings either in isolation or as clusters in many cities. The effects of the wakes behind these high-rise buildings and their interactions with lower buildings were the focus of recent wind-tunnel studies (Park et al. 2015; Aristodemou et al. 2018; Hertwig et al. 2019; Mo et al. 2021), which provide a strong motivation to investigate urban RSL flows over real urban canopies characterized by high-rise buildings.

To study real urban canopies, experimental or numerical approaches can be employed. However, experimental studies of turbulence in the RSL over real urban canopies (Grimmond and Oke 1999; Eliasson et al. 2006; Christen et al. 2007, 2009; Ramamurthy et al. 2007; Wang et al. 2014; Ramamurthy and Pardyjak 2015; Mo et al. 2021) are often hindered by the limitations associated with performing thorough measurements in the field (i.e., measurements are only taken at a few points in space). As a result, spatially averaged

quantities are often unknown and need to be approximated (Christen et al. 2009). Fortunately, state-of-the-art modelling techniques such as large-eddy simulation (LES) offer the opportunities to comprehensively examine the spatiotemporal variability of RSL flows over real urban canopies. Using LES over real canopies, Kanda et al. (2013) found that the standard deviation of building heights and the maximum building height, in addition to the mean building height, were also relevant for the parameterization of spatially averaged flow statistics. Several other LES studies also feature real urban canopies (e.g., Xie and Castro 2009; Giometto et al. 2016, 2017; Efthimiou et al. 2017; Auvinen et al. 2020) but the range of building heights in these studies is often limited. For example, the maximum building height is three times the mean building height in Auvinen et al. (2020) and four times in Giometto et al. (2016, 2017).

In view of these knowledge gaps, this study aims to use LES to simulate flows within and over a real urban canopy in the City of Boston, Massachusetts, USA, which is characterized by a wide range of building heights with maximum building height of about twelve times the mean building height. As a preliminary step towards developing parameterizations for dispersive fluxes, we study the temporally and spatially averaged flow fields and the dispersive fluxes, including their sensitivities to the temporal and spatial averaging scales as well as the grid resolution. We further quantify the spatial structure of dispersive fluxes using quadrant analysis, which is commonly used to study turbulent fluxes. The paper is organized as follows: the concept of dispersive fluxes and the quadrant analysis approach are introduced in Sect. 2; Sect. 3 describes the LES model and its evaluation; Sect. 4 presents the results and conclusions are drawn in Sect. 5.

2 Theoretical Background

2.1 The Double-Averaging Procedure

Due to the spatial heterogeneity of RSL flows and the need to evaluate spatially-averaged quantities, the double-averaging (DA) procedure is often employed (Schmid et al. 2019). The "double-averaging" procedure bears its name from the fact that the averaging operation is conducted along both space and time. The spatial averaging in the DA procedure can be carried out using the intrinsic averaging operation (Nikora et al. 2007),

where the averaging volume (a horizontal slab of arbitrarily small thickness Δz) includes the ambient air only, or the extrinsic averaging (Yuan and Piomelli 2014), where the averaging is performed over the whole horizontal slab (i.e., including the air volume within the buildings). The intrinsic averaging operation is widely used in literature to characterize flow fields over vegetation canopies (Wilson and Shaw 1977; Raupach and Shaw 1982), over gravel beds (Nikora et al. 2007) and rigid canopies (Raupach et al. 1991; Coceal et al. 2006, Xie et al. 2008). Here, we consider the intrinsic spatial averaging of a temporally averaged variable X, defined as:

$$\langle \bar{X} \rangle = \frac{1}{V_f} \iiint \bar{X}(x, y, z) \, \alpha(x, y, z) \, dx dy dz,$$
 (1)

where X is a flow quantity (such as velocity, scalar concentration etc), V_f is the fluid volume, and α is 1 when the space corresponds to the outdoor air and 0 otherwise. The overbar and angular brackets denote time and spatial averaging, respectively. This approach will be used to compute flow statistics including the dispersive fluxes.

2.2 Dispersive Fluxes

Dispersive fluxes, initially introduced by Wilson and Shaw (1977) and Raupach and Shaw (1982), appear as an additional term that represent a contribution to momentum transfer in the doubly-averaged momentum equation. As an illustration, upon applying time and spatial averaging to the product between the vertical velocity w and any flow quantity X, one obtains $\langle \overline{wX} \rangle = \langle \overline{w} \rangle \langle \overline{X} \rangle + \langle \overline{w'X'} \rangle + \langle \overline{w''X''} \rangle$ (Mahrt 1987). Here, prime and double prime denote temporal and spatial deviations, respectively. Namely, $X' = X - \overline{X}$ is the temporal fluctuation of X (i.e., deviations from the temporally-averaged \overline{X}) and $\overline{X''} = \overline{X} - \langle \overline{X} \rangle$ is the spatial deviation of \overline{X} from the spatially averaged \overline{X} . The left-hand side of the equation is the temporally and spatially averaged vertical flux of X, while the terms on the right-hand side of the equation represent the mean or resolved flux, the turbulent flux, and the dispersive flux, respectively. The mean flux is due to time-averaged structures that are larger than the size of the spatial averaging scale. The turbulent flux arises from the temporal correlations in the instantaneous field at any given point, which can be estimated using the temporal eddy-covariance method (i.e., $\overline{w'X'} = \overline{wX} - \overline{w} \, \overline{X}$). In contrast, the

- dispersive fluxes are the result of the spatial correlations of quantities averaged in time but
- varying with space, calculated as $\langle \overline{w}'' \overline{X}'' \rangle = \langle \overline{w} \overline{X} \rangle \langle \overline{w} \rangle \langle \overline{X} \rangle$. In other words, the
- dispersive fluxes naturally appear as the unresolved mean advection or the effect of surface
- heterogeneity on the mean flow.

2.3 Quadrant Analysis

- 178 The classical quadrant analysis provides information on the relationship between the
- temporal fluctuations of velocity components u' and w' (for momentum transport), as well
- as w' and s' (for scalar transport) (Wallace 2016). Here u refers to the streamwise velocity
- and s refers to the scalar concentration. Correlation between these fluctuations reveals the
- presence of turbulent coherent structures that are categorized into outward interaction,
- sweep, inward interaction, and ejection, according to the sign of the fluctuating quantities
- 184 (Shaw et al. 1983; Katul et al. 1997; Li and Bou-Zeid 2011; Wang et al. 2014). In this study,
- dispersive fluxes are investigated by applying quadrant analysis to the spatial deviations of
- time-averaged velocity components (\overline{w}'' and \overline{u}'') and scalar concentration \overline{s}'' . As a result,
- the quadrant analysis applied here aims to reveal the spatially persistent structures of the
- time-averaged flow. This technique has been used to study dispersive fluxes in flows over
- urban-like canopies (Li and Bou-Zeid 2019), rough beds (Pokrajac et al. 2007), rod
- canopies (Poggi and Katul 2008), and plant canopies (Christen and Vogt 2004). Quadrants
- for $\overline{w}''\overline{u}''$ and $\overline{w}''\overline{s}''$ in the (\overline{w}'', u'') -plane and (\overline{w}'', s'') -plane are defined as follows
- 192 (Poggi and Katul 2008):
- Quadrant 1 (Q_1) : $\overline{w}'' > 0$, $\overline{u}'' > 0$ or $\overline{s}'' < 0$ outward interactions (O),
- Quadrant 2 (Q_2): $\overline{w}'' < 0$, $\overline{u}'' > 0$ or $\overline{s}'' < 0$ sweeps (S),
- Quadrant 3 (Q_3) : $\overline{w}'' < 0$, $\overline{u}'' < 0$ or $\overline{s}'' > 0$ inward interactions (I),
- Quadrant 4 (Q_4) : $\overline{w}'' > 0$, $\overline{u}'' < 0$ or $\overline{s}'' > 0$ ejections (E).
- Furthermore, a threshold T_h is defined to separate large, important persistent structures
- from the less important ones, as follows: $|\bar{w}''\bar{u}''| = T_h |\langle \bar{w}''\bar{u}'' \rangle|$. Higher values of T_h
- identify structures with larger absolute values of $\overline{w}''\overline{u}''$ relative to the absolute value of

- dispersive flux $\langle \overline{w}''\overline{u}'' \rangle$. With this threshold, the dispersive flux fraction from each
- 201 quadrant, denoted as F_{i,T_h} , is defined as

$$F_{i,T_h} = \frac{[\overline{w}''\overline{u}'']_{i,T_h}}{\langle \overline{w}''\overline{u}'' \rangle},\tag{2}$$

where the subscript i is the quadrant number and

$$[\overline{w}''\overline{u}'']_{i,T_h} = \frac{1}{V_f} \iiint \overline{w}''\overline{u}''(x,y,z) I_{i,T_h}(x,y,z) \,\mathrm{d}x\mathrm{d}y\mathrm{d}z \tag{3}$$

203 is a conditional average with an indicator function I_{i,T_h} defined as

$$I_{i,T_h} = \begin{cases} 1, & \text{if the point } (\overline{w}'', \overline{u}'') \text{ lies in quadrant } Q_i \text{ and } |\overline{w}''\overline{u}''| > T_h \langle |\overline{w}''\overline{u}''| \rangle \\ 0, & \text{otherwise.} \end{cases}$$

From the above definition of dispersive flux fraction F_{i,T_h} , we obtain

$$\sum_{i=1}^{4} F_{i,0} = 1. (4)$$

The space occupied by quadrant Q_i is called the space fraction S_{i,T_h} , defined as

$$S_{i,T_h} = \frac{1}{V_f} \iiint I_{i,T_h}(x, y, z) \, dx dy dz.$$
 (5)

- The dispersive flux fraction F_{i,T_h} in Eq. 2 and the space fraction S_{i,T_h} in Eq. 5 for scalars
- are defined similarly by replacing \bar{u}'' with \bar{s}'' .

208 **3 Methodology**

- 209 3.1 Large-eddy Simulation Framework
- The LES has become an indispensable tool for studying the atmospheric boundary layer.
- 211 It resolves the large turbulent motions that are mostly responsible for momentum and scalar
- transfer and thus only requires a parameterization for the effect of small-scale turbulence.
- 213 For this study, the PALM model system in revision 4901 (Maronga et al. 2015, 2020) is
- used. The PALM model system has been widely used to study urban flows over both
- idealized (Letzel et al. 2008; Park et al. 2012; Gronemeier et al. 2019; Nazarian et al. 2020;

Blunn et al. 2022) and real urban canopies (Kanda et al. 2013; Park et al. 2015; Gronemeier et al. 2017; Auvinen et al. 2020; Kurppa et al. 2020) and has been validated extensively (Fröhlich and Matzarakis 2020; Gronemeier et al. 2021; Resler et al. 2021).

The PALM solver numerically integrates the filtered, Navier-Stokes equations for incompressible and Newtonian fluids in the Boussinesq-approximations form. For this study, a neutrally stratified environment is assumed, and Coriolis related terms are negligible. To close the system of filtered equations, PALM employs the 1.5-order subgrid scale model of Deardorff (1980). Temporal discretization is done with the 3rd order Runge-Kutta scheme and a predictor-corrector approach, where the divergence generated by the predictor step is corrected via the solution of the Poisson equation for the pressure field. The Poisson equation is solved using an iterative multigrid scheme (Hackbusch 1985), while the 5th order Wicker-Skamarock and the 2nd order central difference schemes are employed to discretize the advection and diffusion schemes. The domain is spatially discretized using the finite difference approach on Arakawa staggered C-grid (Arakawa and Lamb 1977). For more details, we refer readers to Maronga et al. (2015, 2020).

3.2 Evaluation of the PALM Model for Idealized Urban Canopy Flows

Before investigating flows over real urban canopies, it is important to evaluate the predictive capabilities of the PALM model. For this purpose, we adopt a simple configuration with staggered array of cubes (see Fig. 1), similar to that used in previous work such as Coceal et al. (2006), Li and Bou-Zeid (2019) and Tian et al. (2021). We choose this simple configuration because it has been well studied so our results can be compared to previously reported experimental and numerical data. The flow is driven by a negative pressure gradient, whose magnitude and direction are adjusted such that $\langle \overline{u}(z=\delta) \rangle \approx 3.5 \text{ m s}^{-1}$ where $\delta = 9H$ is the boundary layer height and H=12.48 m is the height of cubes. The dimension of the computational domain is $3\delta \times 1.5\delta \times \delta$ with $N_x=216$, $N_y=108$ and $N_z=72$, where N_x , N_y , N_z are the number of grid points in the streamwise, spanwise and vertical direction respectively. A horizontal and vertical grid spacing of $\Delta = H/8$ is used, which is justified based on the grid spacing comparison ($\Delta = H/8$, H/16, H/32) performed by Xie and Castro (2006) for staggered cube array. They showed that LES of turbulent flows over urban-like canopy has a weak dependence on grid

spacing because the total surface drag is mostly pressure drag (i.e., drag caused by the presence of the cube) and the scale of turbulence production processes is comparable to the cube size. Also our computational domain and grid spacing are similar to those used in Li and Bou-Zeid (2019). No slip wall boundary conditions are used at the floor or cube surfaces. Between the surface (including vertical walls) and the first computational grid-level, a constant flux layer with momentum roughness length $z_0 = 0.01$ m is used. Periodic boundary conditions are imposed in the lateral directions to simulate an infinite array of cubes while the top boundary is impermeable with zero stress. The Reynolds number based on friction velocity u_* , height H and air kinematic viscosity v (assuming $v = 1.47 \times 10^{-5}$ m² s⁻¹) is 1.53×10^5 . The friction velocity u_* is evaluated from the total surface drag per unit floor area τ_* , i.e., $u_* = \sqrt{\tau_*/\rho} = 0.18$ m s⁻¹, where ρ is the air density (1 kg m⁻³) and τ_* is the sum of ground floor drag and the total cube (form and skin-friction) drag (Kanda et al. 2013).

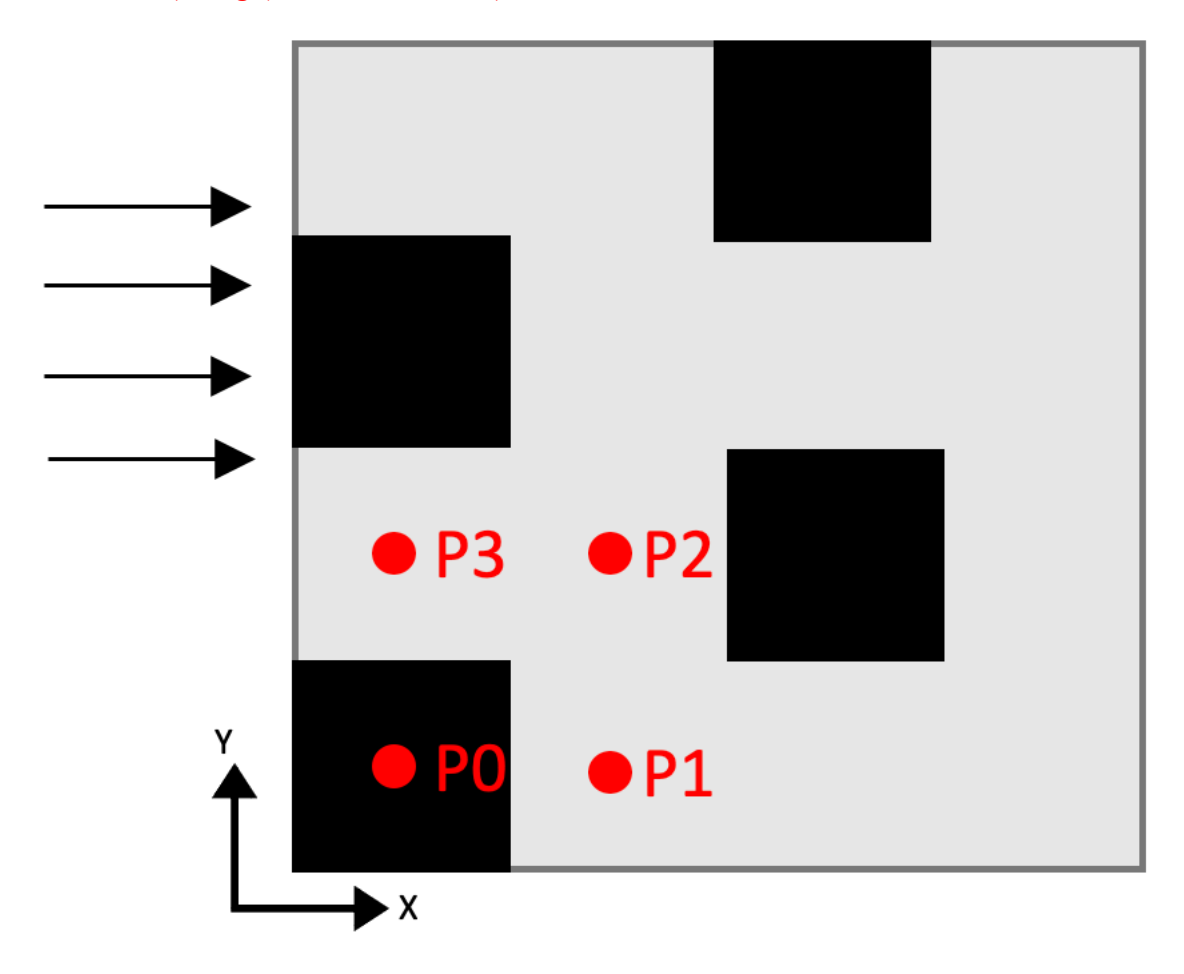


Fig. 1 The plan view of canopy configurations used for PALM evaluation where P0 – P3 are at the 'top', 'behind', 'in front' and 'in between' the cubes. The computational domain consists of 5 by 4 cubes and only a subsection (or a repeating unit) of the domain is shown here

259

260

261

262

263

264

265

266

267

268

269

270

271

272

273

274

275

276

277

278

279

280

281

282

283

284

285

286

287

288

The simulation is initially run for 200 T where $T = H/u_*$ in order to reach a statistical steady state. This duration is the same as the one reported in Li and Bou-Zeid (2019) but longer than the one reported in Coceal et al. (2007a, b). The simulation is then continued for another 200 T to compute the flow statistics. Figure 2 presents the vertical profiles of the mean streamwise velocity normalized by the friction velocity at four positions (P0 to P3, as indicated in Fig. 1). Note that the result at each position is the average of 20 (5 times 4) profiles because the computational domain consists of 5 by 4 cubes. Previously reported LES results of Tian et al. (2021) and direct numerical simulation (DNS) results of Coceal et al. (2007b) are shown for comparison. Moreover, two experimental datasets generated by Particle image velocimetry (PIV) (Blackman and Perret 2016; Blackman et. al. 2017) and laser-Doppler-velocimetry (LDV) (Castro et al. 2006) are shown. The LES runs of Tian et al. (2021) were carried out at a finer grid resolution of H/32 for $z \le 1.5H$ with a refinement of H/64 on all surfaces and down to H/128 at the top of all cubes. PIV datasets were extracted at positions P0 to P3 without spatial averaging and normalized by the friction velocity obtained from drag-force measurements. All datasets (numerical and experimental) presented for comparison in this study are extracted from figures presented in Tian et al. (2021). As can be seen in Fig. 2, the PALM results (black solid lines) are in good agreement with LES data from Tian et al. (2021), DNS data from Coceal et al. (2007b) and wind-tunnel measurements performed by Castro et al. (2006) at the four positions. The PALM results also agree with observations of Blackman et al. (2017) using PIV within the canopy. As reported in Tian et al. (2021), the discrepancies with the PIV measurements of Blackman et al. (2017) above the canopy may be caused by the differences in the boundary-layer height δ . Close inspection of the simulated streamwise velocity profiles indicates that there is an inflection point at z = H over P1, P2 and P3 (see Figs. 2a - c). The actual values of the velocity gradient at the inflection point vary from point to point (it is the largest at P1), which highlights the spatial variation in the local shear layer at the top of the cubes.

Figures 3a, c, e show the vertical profiles of turbulent momentum flux (including the subgrid scale contribution) at three positions. The turbulent momentum flux from z/H =0.3 to the top of the canopy at positions P1 and P2 agrees quite well with LES data from Tian et al. (2021), DNS data from Coceal et al. (2007b) and wind-tunnel measurements performed by Castro et al. (2006) (see Fig. 3a, c). For all positions, the maximum turbulent momentum flux is located near z = H in both simulations and experiments. At position P1 (at the back of the cube), the numerical simulations underestimate this maximum in comparison with the experimental data of Castro et al. (2006) but overestimate this maximum when compared to the PIV data (see Fig. 3a). Consistent with this, the simulated peak values for the standard deviation of vertical velocity σ_w lie between the two experimental datasets (see Fig. 3b). These discrepancies were also found in Tian et al. (2021) and Reynolds and Castro (2008). The first cause of these deviations, as proposed by Reynolds and Castro (2008), is the difference in the ratio of H/δ . The datasets in Fig. 3 have different values of H/δ . We note that our $H/\delta = 11\%$ is close to the $H/\delta =$ 12.5% used in Tian et al. (2021) and Coceal et al. (2007b), and $H/\delta = 13\%$ in Castro et al. (2006). This value differs from $H/\delta = 4.5\%$ used in Blackman et al. (2017). The second cause of these discrepancies is the resolution as the peak value is smoothed out when a coarse resolution is used (Scarano and Riethmuller 2000). Note that the vertical resolution of the PALM run ($\Delta/H = 0.125$) is coarser than both the numerical simulations of Tian et al. (2021) and Coceal et al. (2007b), and the experimental datasets of Castro et al. (2006) and Blackman et al. (2017). At position P2, the vertical profiles of the turbulent momentum flux and σ_w again fall between the two experimental datasets. At position P3, the only available numerical simulation result is the LES data from Tian et al. (2021) and the only available experimental dataset is the PIV from Blackman et al. (2017). The simulated turbulent momentum flux and σ_w agree with the LES data from Tian et al. (2021) over $0.3 \le z/H \le 1.5$. However, the simulated turbulent momentum flux only agrees with the PIV data over $z/H \ge 0.6$ and the simulated σ_w deviates strongly from the PIV data.

289

290

291

292

293

294

295

296

297

298

299

300

301

302

303

304

305

306

307

308

309

310

311

312

313

314

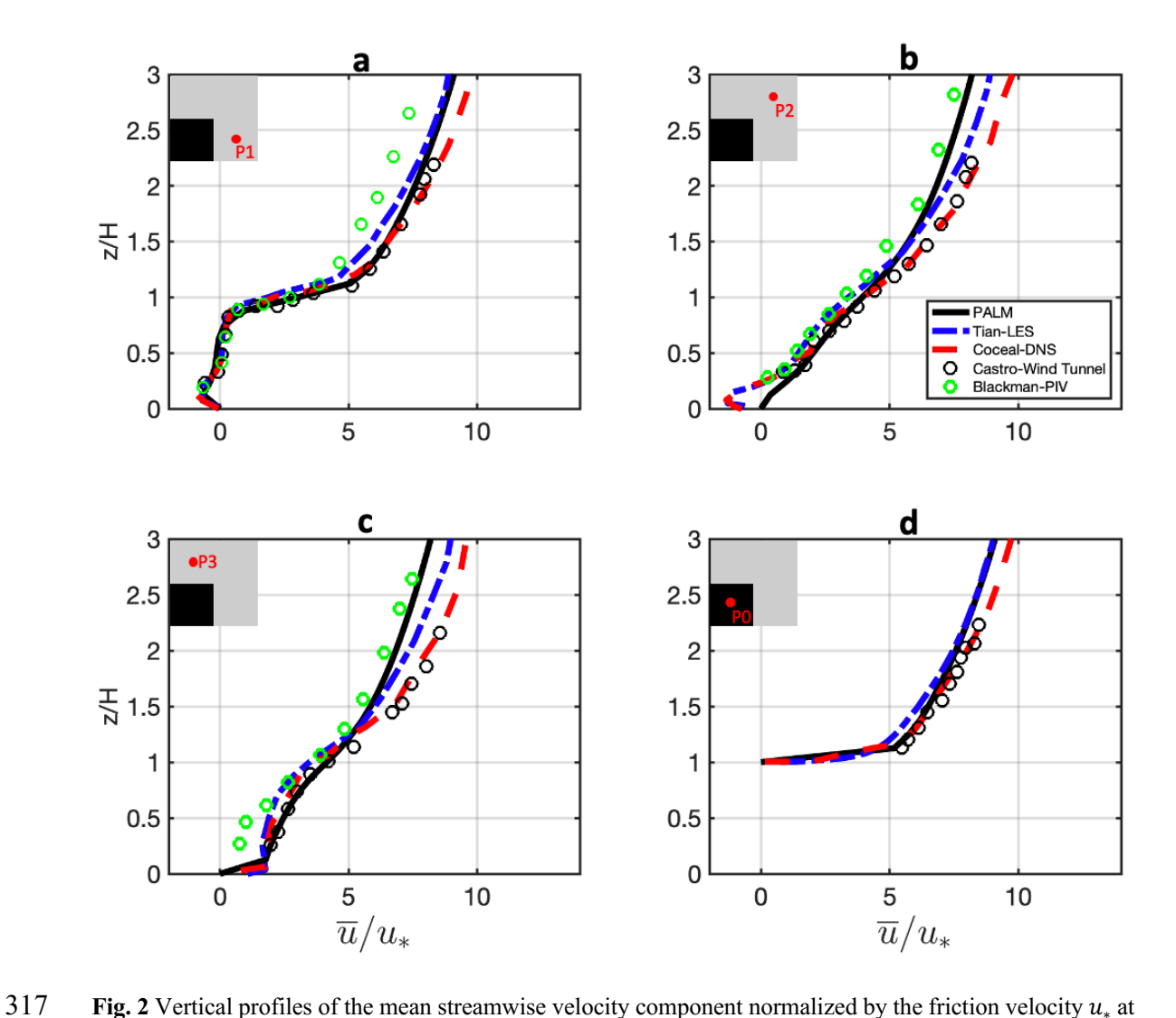


Fig. 2 Vertical profiles of the mean streamwise velocity component normalized by the friction velocity u_* at position a P1, b P2, c P3, and d P0. Black solid line: PALM computations; Blue solid line: LES data from Tian et al. (2021); Red dashed line: DNS data from Coceal et al. (2007b); Black circles: wind-tunnel data from Castro et al. (2006); Green circles: PIV data from Blackman et al. (2017)

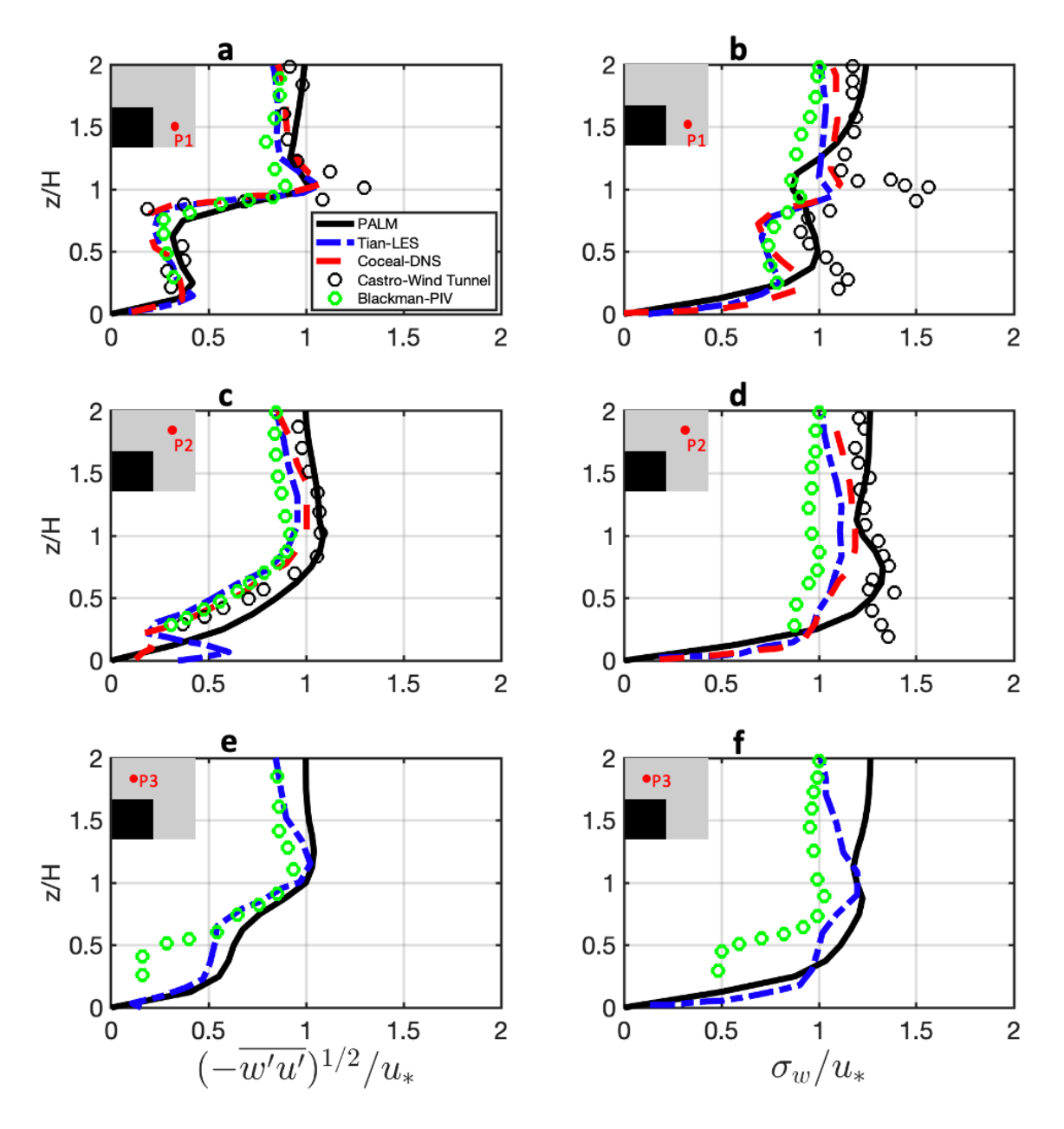


Fig. 3 Vertical profiles of normalized turbulent momentum flux and standard deviation of vertical velocity at position **a, b** P1; **c, d** P2; and **e, f** P3. Black solid line: PALM computations; Blue solid line: LES data from Tian et al. (2021); Red dashed line: DNS data from Coceal et al. (2007b); Black circles: wind-tunnel data from Castro et al. (2006); Green circles: PIV data from Blackman et al. (2017)

Figure 4 presents the standard deviations of streamwise velocity (σ_u) and spanwise velocity (σ_v). In general, larger discrepancies exist between the numerical simulations and the experimental data at all positions when compared to the results shown in Fig. 3. This

is because the standard deviations of horizontal velocity components, especially σ_v , are notoriously difficult to measure and simulate (Tian et al. 2021). The resolution of the simulation also plays an important role. At position P1, the σ_u simulated by PALM model agrees with the LES data from Tian et al. (2021) and experimental datasets from Castro et al. (2006) and Blackman et al. (2017) around the canopy top but deviates elsewhere (see Fig. 4a). Interestingly, the PALM results seem to agree better with the wind-tunnel data than the other two simulations within the canopy but are worse above the canopy at position P1. At positions P2 and P3, the σ_u from the PALM model deviates from the LES data of Tian et al. (2021) but agrees better with wind-tunnel data from Castro et al. (2006), especially above the canopy.

In summary, the PALM model results of both first- and second-order moments show overall good agreement with previous numerical and experimental data. In the following, we use it to study RSL flows over a real urban canopy.

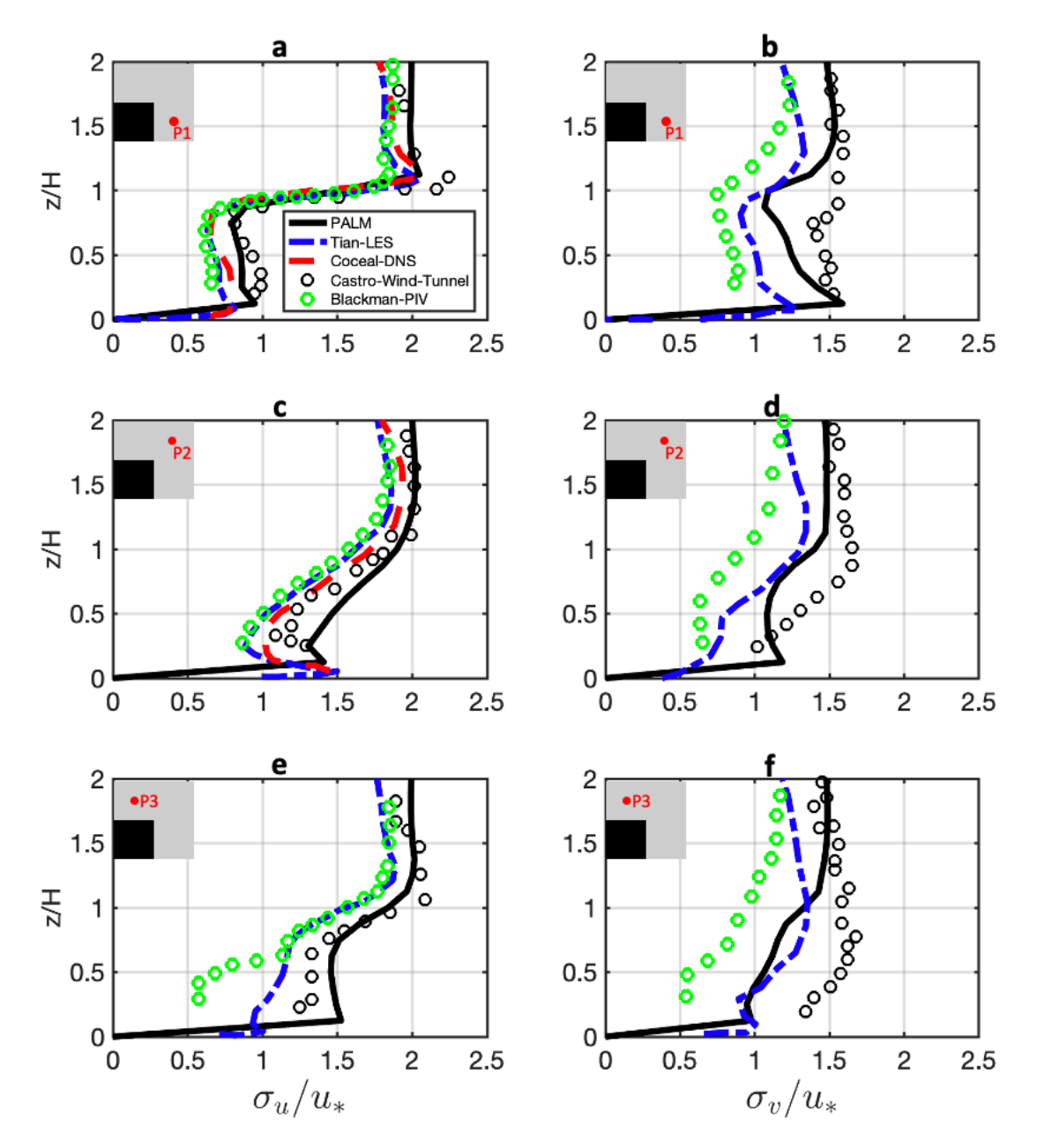


Fig. 4 Vertical profiles of the standard deviation of the streamwise and spanwise velocity component at position **a, b** P1; **c, d** P2; and **e, f** P3. Black solid line: PALM computations; Blue solid line: LES data from Tian et al. (2021); Red dashed line: DNS data from Coceal et al. (2007b); Black circles: wind-tunnel data from Castro et al. (2006); Green circles: PIV data from Blackman et al. (2017)

3.3 Description of the Urban Building Height Dataset

345

346

347

348

349

350

351

352

353

354

355

356

357

358

359

360

361

362

363

364

We begin our investigation of RSL flows over real urban canopies with a description of the building height distribution in our study area (see Fig. 5), which is a $2.4 \times 2.4 \text{ km}^2$ area around Fenway-Kenmore square in the City of Boston, Massachusetts, USA. This area features a dense arrangement of residential blocks, an irregular distribution of narrow street canyons, a park in the northwest region and the Charles River in the north. The northeastern region is a business district with many high-rise buildings of height above 100 m (e.g., the Prudential centre which is 227 m high), while the southwestern region is the home to several hospitals (Boston children hospital, Beth Israel Medical centre, Brigham and Women's hospital) and universities (Harvard school of public health, Emmanuel college, Simmons university and Massachusetts College of Pharmacy and Health Sciences) with moderately tall buildings of about 60 - 80 m in height. Within the study area, the mean building height H is 19 m, the standard deviation σ_H is 17 m, and the plan area fraction $\lambda_p = A_p/A_{\text{total}} = 0.25$, where A_p is the planar area of urban buildings at the ground level and A_{total} is the total planar area of the domain. Note that in previous studies like Auvinen et al. (2020), the building height distribution is almost symmetric with $\sigma_H/H = 0.4 - 0.6$ while Giometto et al. (2016, 2017) studied a building height distribution which was trimodal with $\sigma_H/H = 0.42$. In our study, the distribution is distinctly skewed with $\sigma_H/H = 0.89$. We do not include vegetation, which is justified by its small plan area fraction (Giometto et al. 2016).

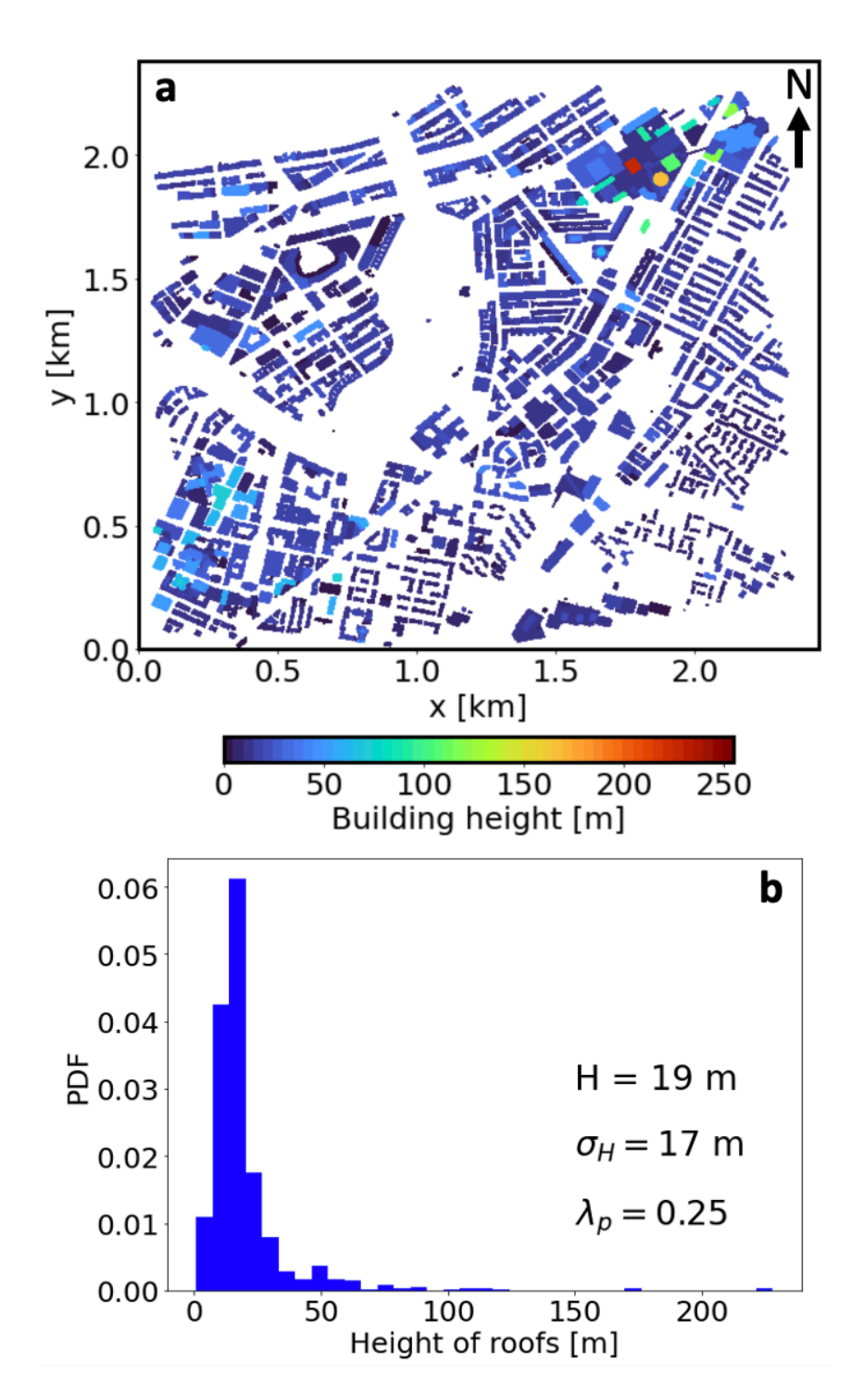


Fig. 5 a Map of the building heights in the study area, with the Charles River in the north, the Boston children hospital (about 75 m) in the southwest, and the Prudential centre (maximum building height of 227 m) in the northeast. **b** Normalized fraction of building heights

3.4 Simulation Setup

For the simulation we adopt a set-up similar to that of Auvinen et al. (2020) and Resler et al. (2021) as shown in Fig. 6. To save computational resources, the self-nesting feature of PALM is utilized (Hellsten et al. 2021). Here self-nesting means that a finer resolution domain (also called child domain) is defined inside a larger but coarser resolution domain (or parent domain). These two model domains run simultaneously with one-way nesting. That is, the simulation in the child domain receives its boundary conditions from the parent domain but does not affect the simulation in the parent domain. The parent domain is $L_x^p =$ 13.82 km, $L_v^p = 3.45$ km and $L_z^p = 1.15$ km while the child domain is $L_x^c = 2.88$ km, $L_{\rm v}^{\rm c}=2.88~{\rm km}$ and $L_{\rm z}^{\rm c}=0.57~{\rm km}$ in the streamwise, spanwise and vertical directions, respectively. The superscripts "p" and "c" denote the parent and child domains, respectively. The child domain starts from x = 9.40 km and y = 0.29 km in the parent domain. The parent domain is discretized with an isotropic grid spacing of 8 m (i.e., Δz^p = 8 m) while the child domain has a grid spacing of 4 m (i.e., $\Delta z^c = 4$ m). The sensitivity of the flow statistics to the resolution of the child domain is presented in Sect. 4.2.3.

For the parent domain, a cyclic boundary condition is applied at the spanwise boundaries while non-cyclic conditions are set at the streamwise boundaries. This is different from many other studies where cyclic boundary conditions were used for all lateral boundaries (Kanda et al. 2013; Giometto et al. 2016, 2017; Inagaki et al. 2017; Gronemeier et al. 2021). The use of non-cyclic boundary conditions along the streamwise direction ensures that the building-induced turbulence is not recycled into the analysis region, which is especially important when dealing with horizontally inhomogeneous surface morphologies such as the one considered herein. The inlet boundary condition is created to mimic a fully developed, homogeneous, neutral boundary layer, which is not affected by buildings downstream. This is achieved with the turbulence recycling technique based on the method by Lund et al. (1998) with modification of Kataoka and Mizuno (2002). This technique has been applied to spatially developing LES of many engineering and environmental flows (Wu 2017; Wang et al. 2021).

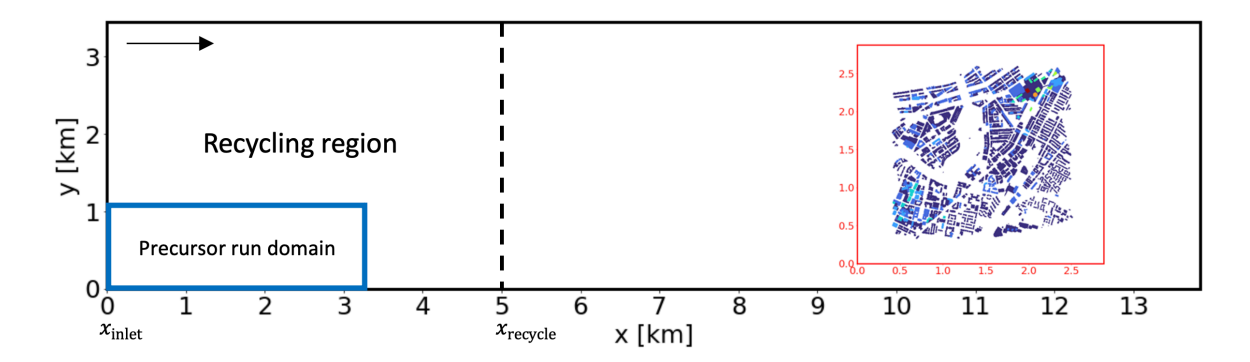


Fig. 6 The model set-up. The solid black line shows the horizontal extent of the parent domain while the red solid line on the right is the child domain and the region where all statistics are computed. The horizontal extent of the precursor simulation domain, used to initialize both domains, is shown in the bottom left corner of the parent domain in blue. The left corner of the parent domain features the recycling region. The black arrow at the top left corner indicates the wind direction

397

398

399

400

401

402

403

404

405

406

407

408

409

410

411

412

413

414

415

416

417

418

419

The implementation of this boundary condition on the parent domain in PALM is presented in Maronga et al. (2015) and it is discussed here with modified notation to make this paper self-contained. The inlet boundary value of a prognostic variable $\phi =$ $\phi(x, y, z, t)$, where $\phi \in \{u, v, w, s, e\}$, is constructed from its temporally and horizontally averaged vertical profiles $\langle \overline{\phi} \rangle(z)$ and the fluctuating components $\phi'(x,y,z,t)$ through $\phi_{\text{inlet}}(x, y, z, t)|_{x=x_{\text{inlet}}} = \langle \overline{\phi} \rangle(z) + \phi'(x, y, z, t)$. The fluctuating component ϕ' is computed from a specified recycling y - z plane at a given streamwise coordinate $x_{\text{recycle}} = 5 \text{ km}$, placed far downstream from the inlet to avoid the feedback of disturbances inlet and the recycling plane. ϕ' is obtained between the $\phi_{\text{recycle}}(x, y, z, t)|_{x = x_{\text{recycle}}} - \langle \phi \rangle_y|_{x = x_{\text{recycle}}}$, where $\langle \phi \rangle_y|_{x = x_{\text{recycle}}}$ is the spanwise mean at $x_{\rm recycle} = 5$ km. Only fluctuations at z < 0.75 $L_z^{\rm p}$ are recycled while fluctuations at z > $0.75~L_z^p$ are damped to zero to prevent the growth of the boundary layer; hence δ is 0.75 L_z^p . The boundary-layer height of the parent domain is $\delta/H = 45$, which almost satisfies the $\delta/H \gtrsim 50$ requirement (Jimenez 2004). The temporally and horizontally averaged vertical profile $\langle \overline{\phi} \rangle(z)$ for the prognostic variable is held fixed at the inlet and is generated from a precomputed simulation, called a precursor run. The domain of the precursor run can be seen in the bottom left corner of Fig. 6 with dimension 3.45 km \times 1.1 km × 1.1 km in the streamwise, spanwise and vertical directions, respectively. The precursor run has the same resolution as the parent domain but with periodic lateral boundary conditions, and free-slip and no-slip conditions at the top and bottom, respectively. The precursor run is driven by a constant initial streamwise velocity of 3.5 m s⁻¹ and zero spanwise velocity. It is then computed for 390 $T_{\text{precursor}}$, where $T_{\text{precursor}} = L_z/\langle \bar{u}(z=\delta) \rangle$. The temporally and horizontally averaged vertical profiles are obtained from the last 150 $T_{\text{precursor}}$. The wind direction is held constant for the precursor and parent runs and is from west to east.

426

427

428

429

430

431

432

433

434

435

436

437

438

439

440

441

442

443

444

445

446

447

448

449

450

A long section of the parent domain before the urban canopy is constructed for two reasons. First, it helps in the development and evolution of large-scale motions and very large-scale motions that are seen in boundary layer flows (Balakumar and Adrian 2007; Chung and McKeon 2010; Hutchins et al. 2012). The presence and relevance of these largescale streamwise structures have been extensively studied (Hutchins and Marusic 2007; Mathis et al. 2009; Anderson 2016). Studies have shown that these structures affect the RSL flows via amplitude modulation, and they are considered a universal trait of boundarylayer flows under neutral conditions (Anderson 2016). The sizes of these large-scale structures are usually in the range $10\delta - 20\delta$ in the streamwise direction (Fang and Porté-Agel 2015). Here, the size of our computational domain in the streamwise direction is about 18δ and hence might accommodate these large-scale structures. Second, the recycling region needs to avoid the disturbances that travel upstream from the edge of the urban canopy. These disturbances can give rise to a weak perturbation at the recycling region, which can be transported to the inlet because of turbulence recycling mentioned earlier. As a result, we limit this effect by increasing the distance between the recycling region and the edge of the urban canopy. Moreover, the turbulence recycling technique is prone to numerically amplify long streamwise disturbances when neutral stratification with no spanwise velocity component is used, causing large-scale structures at the recycling plane to become correlated with those at the inlet (Fishpool et al. 2009). These numerical streaklike artifacts can be eliminated either by introducing a small flow angle to the simulation (Auvinen et al. 2020, Karttunen et al. 2020) or using a shifting method (Munters et al. 2016) to the parent run. In the shifting approach, the velocity at the recycling plane is first shifted uniformly in the spanwise direction by a constant distance d_s before it is reintroduced at the inlet. The parameter d_s should be chosen in a way to avoid reintroducing the same turbulent structure in the same spanwise location after a few

451 flowthroughs. This approach was shown to be effective in breaking up these persistent 452 streaks for developing urban boundary layers (Munters et al. 2016; Gronemeier et al. 2021; Hellsten et al. 2021). We apply the shifting method (using $d_s = 380$ m) to the parent run. 453 454 The simulation is initialized by repetitively copying the precursor run flow solution to 455 the parent and child domains (Maronga et al. 2015). The no-slip wall boundary condition is imposed on all surfaces (including the roofs, ground and building walls) while free-slip 456 457 conditions are applied to the top of the parent domain. To account for the effects of low vegetation and other structural details, a momentum roughness length $z_0 = 0.01$ m is 458 used, which agrees the recommendation of Basu and Lacser (2017) that $z_0 \le$ 459 $0.02 \times \min(\Delta z)$. The value $\min(\Delta z^c) = 2$ m for this study because the first 460 computational level is positioned at $0.5 \Delta z^c$ for the staggered grid. We assume a constant 461 462 flux layer between the surface (including the roofs, ground and building walls) and the first 463 computational grid-level. The boundary condition for passive scalar is a surface flux of $0.05~{\rm kg}~{\rm m}^{-2}~{\rm s}^{-1}$ imposed on all surfaces (including the roofs, ground and building walls). 464 465 After the initialization, the urban simulation runs for a spin-up period of 180 T where T =466 H/u_* in order to reach a steady state. Here T is interpreted as the eddy-turnover time for the largest eddies (Coceal et al. 2006). The friction velocity $u_* = 0.17 \,\mathrm{m \, s^{-1}}$ is again 467 computed from the total surface drag (as defined in Sect. 3.2), which is the sum of the 468 469 friction and pressure drag on the buildings and the friction drag on the ground floor. The 470 pressure drag on the buildings accounts for about 90% of the total surface drag. The 471 simulation is then pursued for another 360 T to compute all temporal averaging statistics. 472 Data analyses are conducted only in the child domain where all statistics are computed. 473 The streamwise velocity, vertical velocity, momentum fluxes and velocity variances are normalized with the friction velocity u_* . The scalar concentration is normalized with $s_* =$ 474 $\overline{w's'}_0/u_*$ where $\overline{w's'}_0 = 0.05 \text{ kg m}^{-2} \text{ s}^{-1}$ is the surface scalar flux. The scalar fluxes are 475 476 normalized with u_*s_* . The vertical height is normalized with the mean building height 477 (H = 19 m).

4 Results and Discussion

4.1 Instantaneous Velocity and Scalar Concentration

Figures 7 and 8 display the instantaneous streamwise velocity, vertical velocity, and scalar concentration. As can be seen, the RSL flow is strongly affected by the heterogeneity of the urban canopy and is characterized by a wide range of length scales. The relatively large ratio between the standard deviation of building heights and the mean building height ($\sigma_H/H = 0.89$) causes the flow to alternate between different flow regimes such as skimming and wake interference (see Oke (1988) for the definition of flow regimes). Wake and non-wake regions can clearly be identified in the RSL (see Fig. 7 a) (Bohm et al. 2013) while the flow contains high and low momentum streamwise elongated streaks within the inertial sublayer (see Fig. 7b) (Inagaki et al. 2012; Giometto et al. 2016). The existence of these large streaky structures over urban areas is expected as reported by Inagaki et al. (2012).

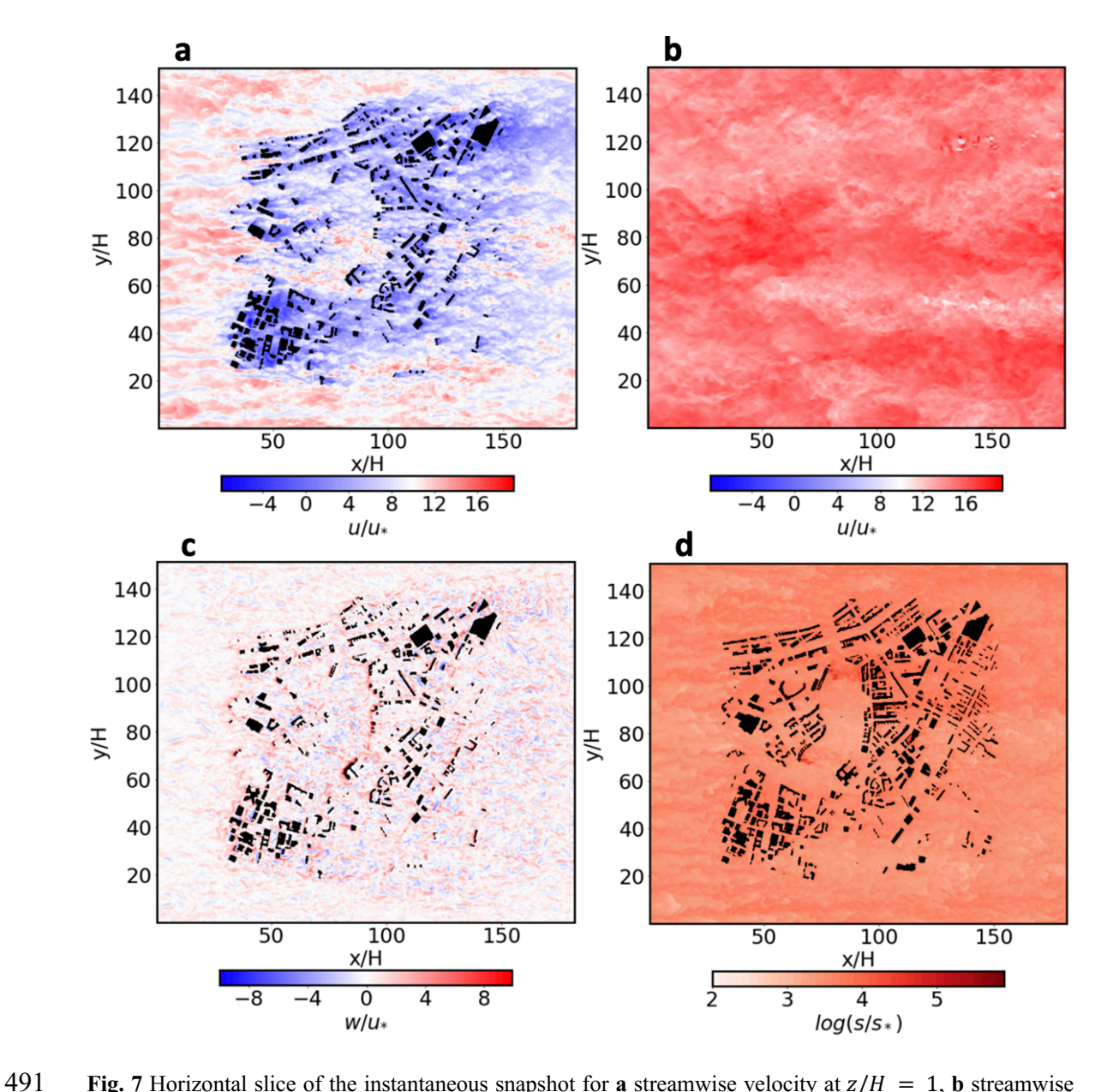


Fig. 7 Horizontal slice of the instantaneous snapshot for **a** streamwise velocity at z/H = 1, **b** streamwise velocity at z/H = 13, **c** vertical velocity at z/H = 1 and **d** logarithm of the scalar concentration at z/H = 1. Streamwise and vertical velocity are normalized by the friction velocity u_* while the scalar concentration is normalized by s_* . The x- and y- axis are defined in terms of the child domain

Elongated wakes with a streamwise extent of about 0.5 – 1 km are found behind high-rise buildings (see Fig. 8 a). The vertical velocity shows regions of updrafts mostly at the windward side of the buildings, efficiently transporting passive scalars to the upper part of the RSL while downdrafts are seen at the leeward side of the building (see Figs. 7c and 8b). The presence of high-rise buildings causes strong updrafts at its windward side. The

leeward side contains two distinct regions of the building wake: the momentum deficit in the main wake and the recirculation zone in the near wake, consistent with the study of Hertwig et al. (2019). The wake can extend downward and interact with lower buildings (see Fig. 8). The scalar concentration mostly peaks in low-speed regions especially in areas where there are building clusters or at the wake of high-rise buildings (see Fig. 7 d), which agrees with Aristodemou et al. (2018). These results are consistent with the literature that shows the importance of high-rise buildings in affecting urban RSL flow structures (Flaherty et al. 2007; Xie and Castro 2009; Cheng et al. 2021; Mo et al. 2021).

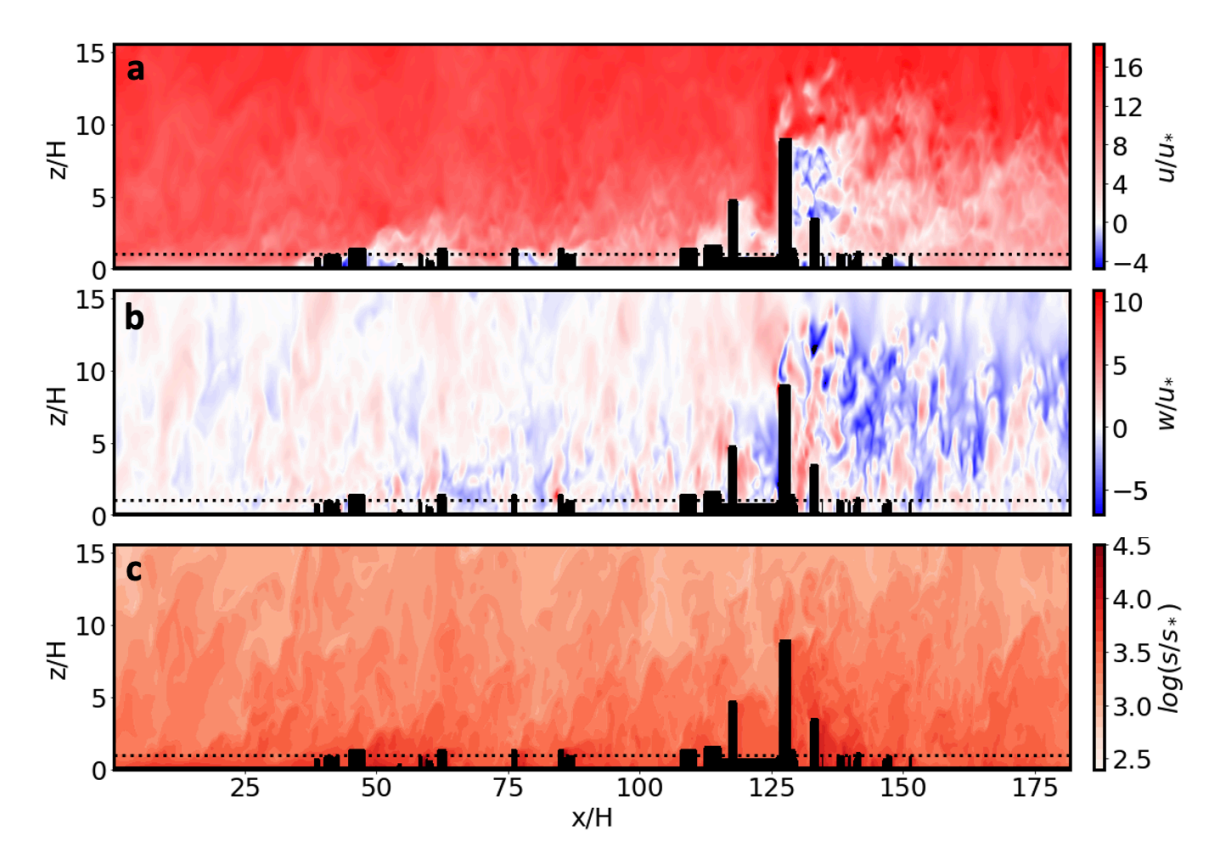


Fig. 8 Vertical slice of the instantaneous snapshot for a streamwise velocity, b vertical velocity and c logarithm of the scalar concentration at y/H = 116. Streamwise and vertical velocity are normalized by the friction velocity u_* while the scalar concentration is normalized by s_* . The dashed horizontal line indicates the height z/H = 1. The x- axis are defined in terms of the child domain

4.2 Double-Averaging Flow Statistics in the Roughness Sublayer

The double-averaging (DA) approach described in Sect. 2.1 is used to compute the flow statistics. For the DA profiles presented in this study, the time averaging is performed first,

followed by the intrinsic spatial averaging over horizontal slabs of thickness Δz^c (i.e., using Eq. 1). Figure 9 presents the double-averaging profiles of streamwise velocity, vertical velocity, and scalar concentration and their variances below z/H = 30. The reason we focus on the region below z/H = 30 is that the dispersive momentum flux does not disappear until z/H = 30, as shall be seen later.

515

516

517

518

519

520

521

522

523

524

525

526

527

528

529

530

531

532

533

534

535

536

537

538

One outstanding feature is that there is no inflection point in the mean streamwise velocity profile. This is in contrast with previous studies on vegetation canopy (Raupach et al. 1996), urban-like canopy flows (Li and Bou-Zeid 2019), and real urban canopy with smaller σ_H (Giometto et al. 2016, 2017; Auvinen et al. 2020). But this is consistent with the profiles presented in Park et al. (2015) and Inagaki et al. (2017) who also studied real urban canopies with large σ_H values. The reason for this is that the irregularity of the building shape and height induces large vortical wakes that interact with downstream elements, causing significant flow penetration into the urban canopy (Britter and Hunt 1979; Belcher et al. 2003). This interaction prevents the formation of inflection points and could introduce high mixing rates (Makedonas et al. 2021). The variance of streamwise velocity has its maximum below H (around z/H = 0.5) and then decreases with increasing height. The maximum of the vertical velocity at the maximum building height, which corresponds to z/H = 12, shows the presence of strong updrafts mostly induced by high rise buildings (see Fig. 8b). The variance of the vertical velocity peaks slightly above H (around z/H = 2.5), which is about five times the height of the maximum peak of $\langle \overline{u'^2} \rangle$. The maximum turbulent kinetic energy is 4.59 u_*^2 seen around z/H = 0.5 (see Fig. 9f) and decreases with increasing height. The DA profile of the logarithm of scalar concentration indicates a strong mixing of passive scalar from urban surfaces where it is released to the atmosphere when compared with the scalar initial profile (not shown).

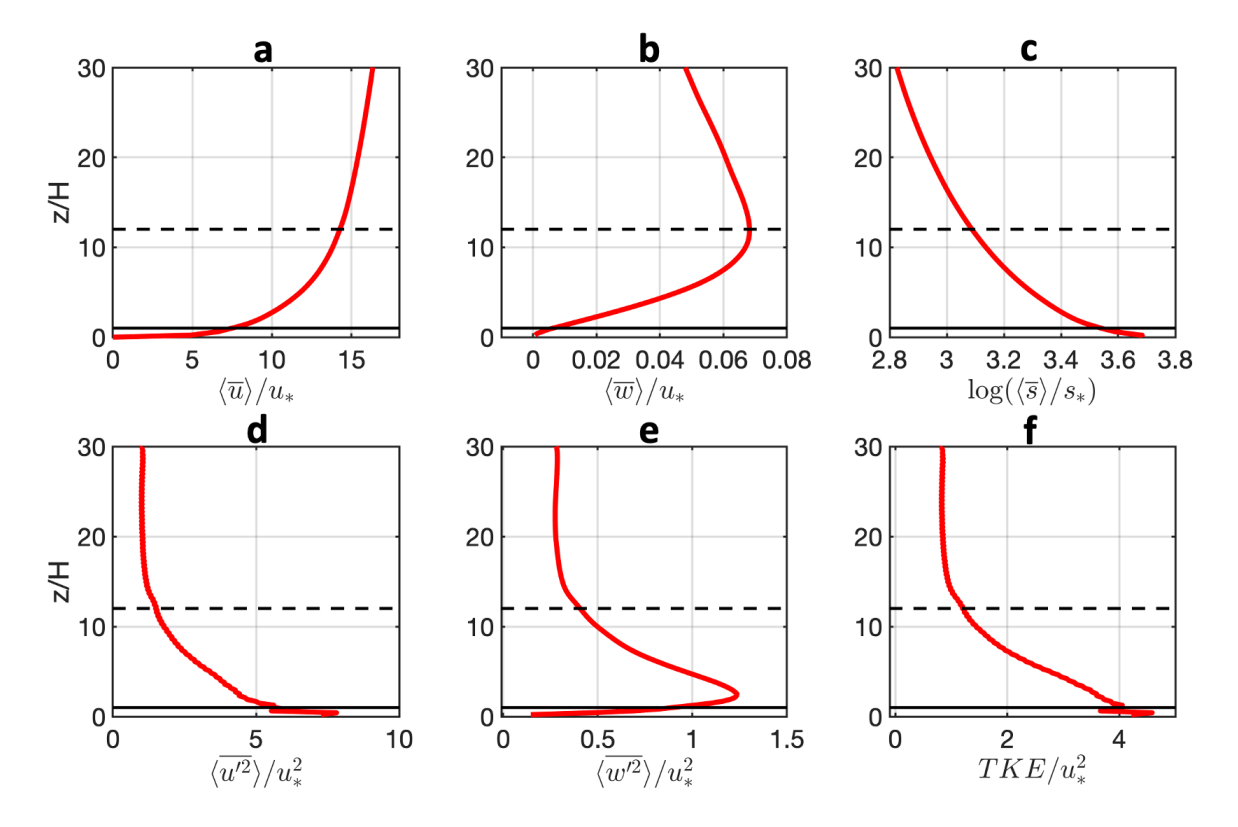


Fig. 9 Normalized DA profiles of a streamwise velocity, **b** vertical velocity, **c** logarithm of the scalar concentration, **d** variance of streamwise velocity, **e** variance of vertical velocity, and **f** turbulent kinetic energy $TKE = 0.5(\langle \overline{u'^2} + \overline{v'^2} + \overline{w'^2} \rangle)$. Momentum and TKE profiles are normalized with the friction velocity u_* while the scalar profile is normalized by with s_* . Solid horizontal line indicates the mean building height H while the dashed horizontal line is the maximum building height H_{max}

The mean, turbulent, dispersive fluxes and the ratio of dispersive fluxes to the sum of turbulent and dispersive fluxes for both momentum and scalar are presented in Fig. 10 and 11. Only the resolved parts of the turbulent fluxes are presented since the momentum subgrid scale part is less than 6% of sum of resolved and subgrid scale turbulent momentum flux above z/H = 0.5. The mean momentum flux in Fig. 10a is non-zero as buildings significantly slow down the flow, causing strong vertical motions (Mason 1995). Note that the mean momentum or scalar flux is absent in studies that impose cyclic lateral boundary conditions in both streamwise and spanwise directions. A sensitivity test shows that using non-cyclic boundary conditions in the streamwise direction not only creates a mean momentum or scalar flux, but also affects the dispersive fluxes (not shown). While this is an important technical detail to point out, a full investigation of such differences is left for

the future. In Fig. 10a, the mean momentum flux peaks at H_{max} , which agrees with Cheng et al. (2021), while its scalar counterpart peaks at 0.6 H_{max} (see Fig. 11a). From now on, the mean fluxes will not be discussed further since they are resolved in large-scale meteorological models. The peak turbulent momentum flux, which occurs at z/H = 2, is more than four times its value in the inertial sublayer (see Fig.10b). The same behavior is seen for the turbulent scalar flux, which also peaks at z/H = 2 (see Fig. 11b).

The dispersive momentum flux peaks at z/H = 0.5 with an opposite sign (positive) as the turbulent momentum flux but becomes negative above H_{max} (see Fig. 10c). The positive sign of the dispersive momentum flux below $z = H_{\text{max}}$ deviates from some idealized or realistic urban canopy studies (e.g., Giometto et al. 2016; Coceal et al. 2006) but other idealized studies (such as Nazarian et al. 2020; Blunn et al. 2022) showed that the dispersive momentum flux can be positive below H, especially for flows over aligned cubes with large plan area fractions. The magnitude of the strongest dispersive momentum flux is found to be 0.09 u_*^2 . Below this peak value, which occurs at z/H = 0.5, the dispersive momentum flux increases with height from the surface. The dispersive momentum flux then decreases until it reaches $0.04 u_*^2$ at H. Above H, it increases to another peak value at z/H = 5, with magnitude only slightly smaller than the one at z/H = 10.5. Further up, the dispersive momentum flux decreases with height from this secondary peak (i.e., z/H = 5) and becomes negative at around the maximum building height, its magnitude reaching 10% of the peak value at z/H = 15 and zero at z/H = 30. If we use zero dispersive momentum flux as an indicator of the inertial sublayer, then the height of RSL extends to z/H = 30, which is much higher than other studies with smaller σ_H (Giometto et al. 2016, 2017; Auvinen et al. 2020).

For the dispersive scalar flux, the peak of about $0.35 u_* s_*$ is seen at z/H = 0.5, which is about 35% of the turbulent scalar flux. This is larger than the value (10%) reported by Leonardi (2015) for urban-like canopies. The dispersive scalar flux decreases with height to a negative value at z/H = 5 and then increases until it reaches zero at z/H = 15 (see Fig. 11 c). The main difference observed between the dispersive momentum transport and its scalar counterpart is because of the non-local action of pressure on momentum, which causes the streamwise velocity to decrease at the windward region but does not influence

the transport of scalars (Li and Bou-Zeid 2019). It is clear from these results that the entire building height distribution, including σ_H , influences the vertical variations of turbulent and dispersive fluxes.

The reason for the smaller peak of the dispersive momentum flux compared to $0.15 u_*^2$ reported in Giometto et al. (2016) might be caused by the differences in the morphology of the urban canopy. It may also be due to the spatial averaging scale used, which is four times larger than that in Giometto et al. (2016). In Cheng et al. (2021), the dispersive momentum fluxes were calculated locally over small regions with sizes 300 m \times 350 m. They found that turbulent and dispersive momentum fluxes are comparable below z/H = 4. Comparing these studies raises an important question: what is the sensitivity of dispersive momentum flux to the spatial averaging scale? We will address this question in Sect. 4.2.2.

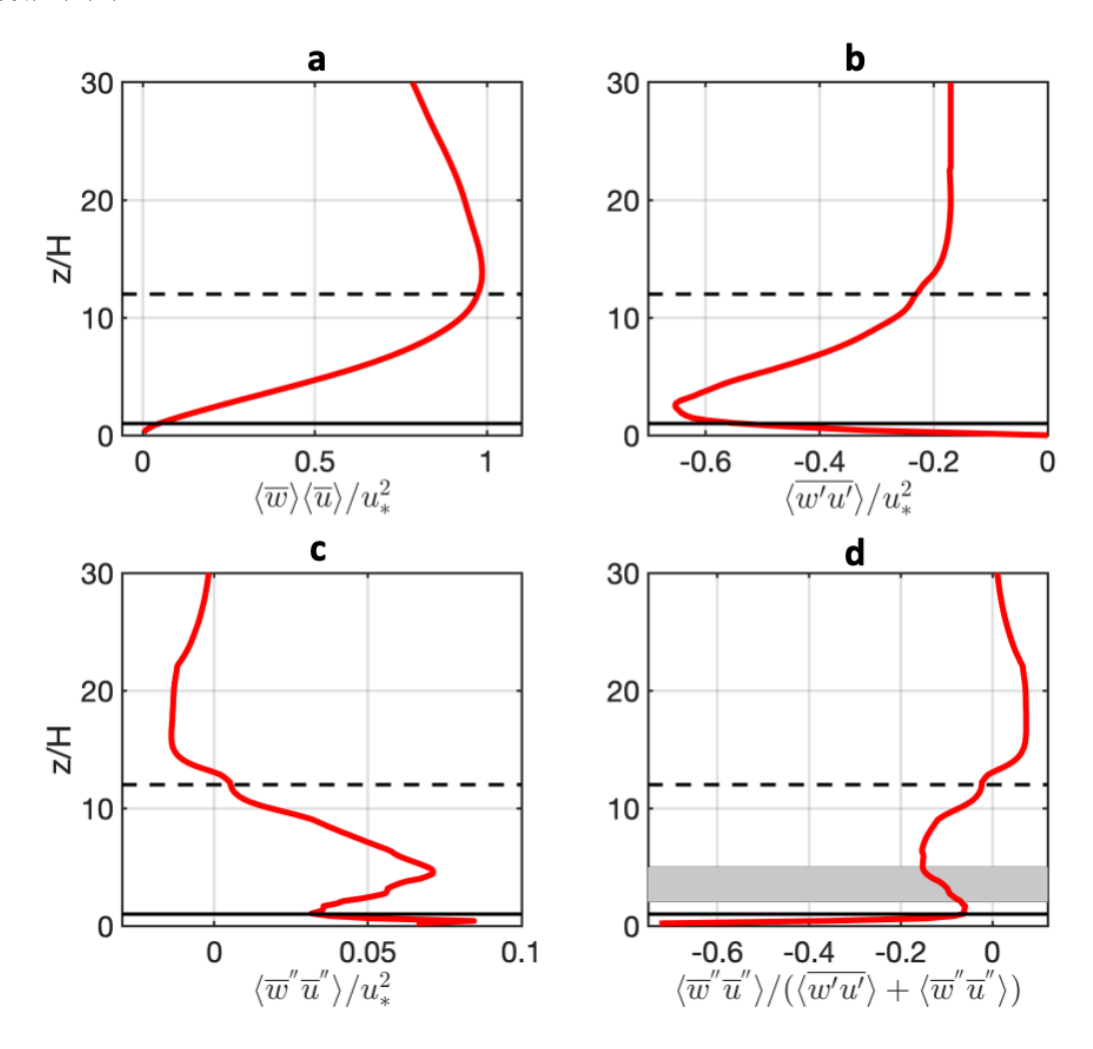


Fig. 10 Normalized DA profiles of a mean momentum flux, b turbulent momentum flux, c dispersive momentum flux d contribution of dispersive momentum flux to the sum of turbulent and dispersive momentum flux. Momentum profiles in a, b and c are normalized by the friction velocity u_* . Solid horizontal line indicates the mean building height H while the dashed horizontal line is the maximum building height H_{max} . Grey region in d corresponds to the values of z/H between 2 to 5

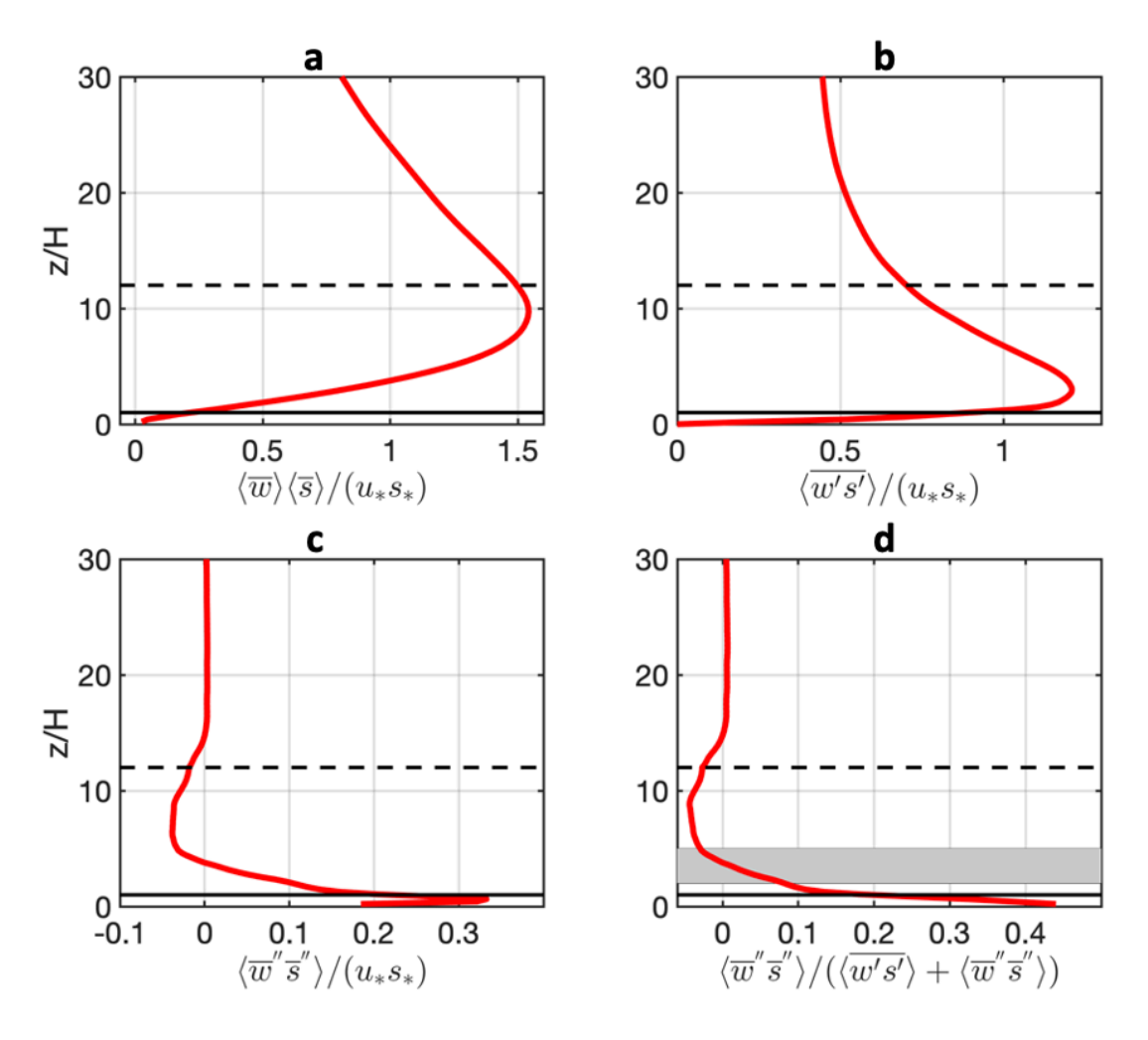


Fig. 11 Normalized DA profiles of **a** mean scalar flux, **b** turbulent scalar flux, **c** dispersive scalar flux and **d** contribution of dispersive scalar flux to the sum of turbulent and dispersive momentum flux. Scalar profiles in **a**, **b** and **c** are normalized by u_*s_* Solid horizontal line indicates the mean building height H while the dashed horizontal line is the maximum building height H_{max} . Grey region in **d** corresponds to the values of z/H between 2 to 5

Figure 10d and 11d show the ratio of dispersive fluxes to the sum of turbulent and dispersive fluxes. Below H, the contribution of dispersive momentum flux decreases with

height from about 75% close to the surface to 10% at H. Between H and H_{max} , its contribution is around 5% to 15 % while above $H_{\rm max}$, it is around 7%. The largest contribution of dispersive scalar flux is found below H (between 20% to 40% of the sum of turbulent and dispersive scalar fluxes) and the dispersive scalar flux becomes zero above z/H = 15 (also around z/H = 4 due to a change of the sign of dispersive scalar flux). This result shows that the dispersive (momentum and scalar) flux within the urban RSL can be significant beyond z/H = 2 - 5 (represented by the grey area in Fig. 10d and 11d), which is often used as an estimate of the urban RSL height by previous studies with uniform height or relatively smaller σ_H (Coceal et al. 2006; Martilli and Santiago 2007; Giometto et al. 2016; Li and Bou-Zeid 2019). This commonly used urban RSL height (z/H = 2 – 5) also roughly corresponds to the typical height of the lowest atmospheric model level (about 30 - 100 m) in weather and climate models. This emphasizes the need to parameterize dispersive fluxes in large-scale meteorological models, due to their contributions to the unresolved momentum and scalar fluxes, even beyond z/H = 2 - 5. The results presented in the remaining part of Sect. 4.2 is normalized with the sum of dispersive and turbulent fluxes to highlight the sensitivity of the contribution of dispersive fluxes to temporal and spatial averaging, as well as the grid resolution.

626 4.2.1 Temporal averaging sensitivity

The strong variability of the building heights can trigger secondary circulations that remain in the urban RSL for a long time. This has been observed by Coceal et al. (2006) and Leonardi et al. (2010, 2015) for flow over staggered cubes. These studies showed that dispersive fluxes (momentum and scalar) are important on intermediate time scales and can become very small when averages are performed over long time scales. It is still unknown whether these findings also apply to real urban canopies. To examine the sensitivity of the contribution of dispersive fluxes to temporal averaging, we apply different averaging time intervals. Figure 12 shows that the profiles of dispersive momentum and scalar fluxes are indeed sensitive to the averaging time interval but converges at about 360 *T*. For this reason, intermediate averaging time interval of 360 *T* is used in the present study. Similar argument was made by Li and Bou-Zeid (2019) to estimate dispersive momentum fluxes over urban-like canopies. Due to the limitation in computational

resources, it is not possible to see if the profile will further change at time scales longer than 720 T.

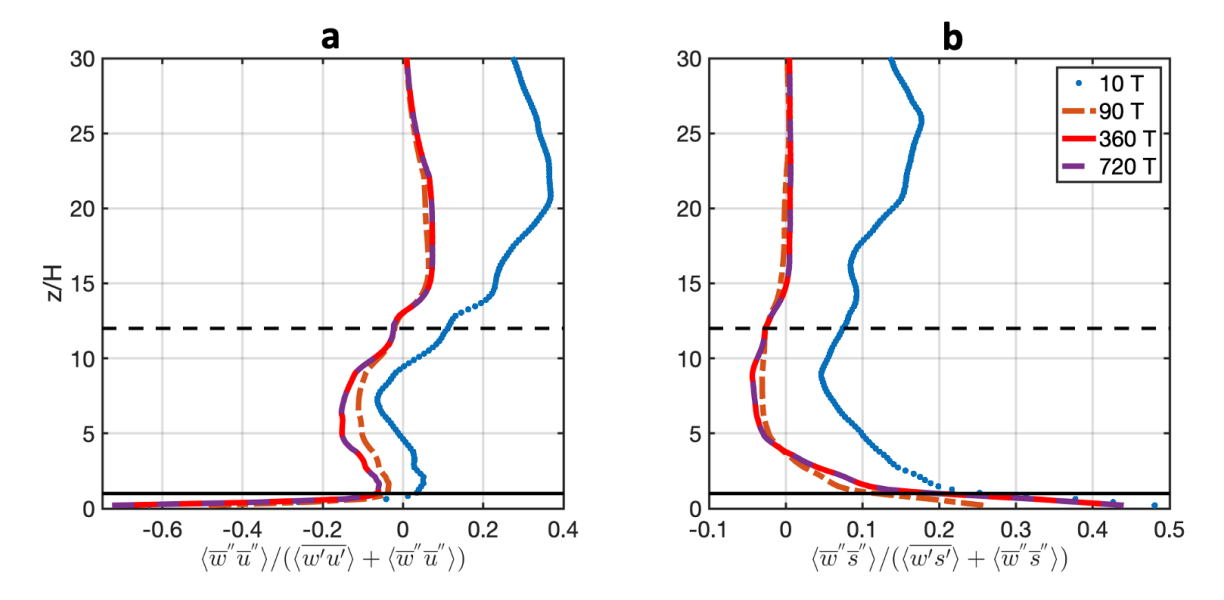


Fig. 12 Normalized dispersive **a** momentum **b** scalar fluxes computed using averaging time intervals of 10 T, 90 T, 360 T and 720 T. The dispersive momentum and scalar fluxes are normalized by the sum of their turbulent and dispersive fluxes. Solid horizontal line indicates the mean building height H while the dashed horizontal line is the maximum building height H_{max}

4.2.2 Spatial averaging sensitivity

As discussed earlier, both time and spatial averaging are required to compute dispersive fluxes. For urban-like canopies of uniform height, the spatial averaging scale over which the dispersive fluxes are calculated will not significantly affect the magnitude of the dispersive fluxes. This is not the case for real urban canopies since the flow statistics strongly depends on the entire building height distribution. In Sect. 4.2, we observed a smaller peak value of dispersive momentum flux compared to previous studies such as Giometto et al. (2016). Also, locally calculated dispersive momentum fluxes by Cheng et al. (2021) were shown to be of similar magnitude as the turbulent momentum flux below z/H = 4 and about 20% to 30% of the turbulent momentum flux above this height. As a result, we hypothesized that one cause of these discrepancies is the difference in spatial averaging scale. In Fig. 13, the sensitivity of the dispersive flux to the spatial averaging scale is shown. Since the flow moves from west to east, the partitioning of the child domain

into subdomains is done to observe how the dispersive fluxes change as the flow moves downstream. To do so, we include subdomains with different streamwise lengths (L_x^c) but covering the whole spanwise length (L_{ν}^{c}) . In the streamwise direction, each subdomain starts from the transition region (i.e., smooth – rough interface) and extends to $L_x^c/4$, $L_x^c/2$ and L_x^c (see Fig. 13). The $L_x^c/2$ subdomain has a mean building height H=19 m, maximum building height $H_{\text{max}} = 74 \text{ m}$, standard deviation of building height $\sigma_H = 13 \text{ m}$ and plan area fraction $\lambda_p = 0.23$ m while the $L_x^c/4$ subdomain has H = 22 m, $H_{\text{max}} = 74$ m, $\sigma_H = 15$ m and $\lambda_p = 0.27$ m. Figure 13 shows that above H, the peak magnitude of the contribution of dispersive momentum flux increases as the streamwise length decreases. Its peak is the largest when the size of the subdomain is close to the transition length scale L_T . The transition length scale L_T is the length scale the turbulent boundary layer needs to adjust to the urban roughness below it (Belcher et al. 2003). Based on the definition of L_T (Belcher et al. 2003), we find $L_T \approx 1$ km and $L_T/L_x^c = 0.3$, which is close to $L_x^c/4$. Note that for the $L_x^c/4$ subdomain, the peak of the dispersive momentum flux is larger than $0.15 u_*^2$ reported in Giometto et al. (2016). For the scalar, only the shape of the profile is affected by the spatial averaging scale. Here it is important to emphasize that the shape of the dispersive momentum and scalar flux profiles depend not only on its streamwise distance from the transition (as demonstrated in this study) or the scale of spatial averaging operation, but also on the urban morphology within the averaging domain. This implies that the plan area fraction λ_p , the frontal area fraction $\lambda_f = A_f/A_{\text{total}}$ (A_f is the product of the building width and height), and the scale of the spatial averaging operation affect the significance of the dispersive momentum and scalar fluxes over real urban canopies. Note that the sensitivity of the dispersive fluxes to variations in λ_f was studied in Li and Bou-Zeid (2019). Despite its relevance for the urban microclimate community, a more detailed investigation on the sensitivity of dispersive fluxes to variations in the aforementioned parameters is beyond the scope of this analysis and is hence left for the future.

658

659

660

661

662

663

664

665

666

667

668

669

670

671

672

673

674

675

676

677

678

679

680

681

682

683

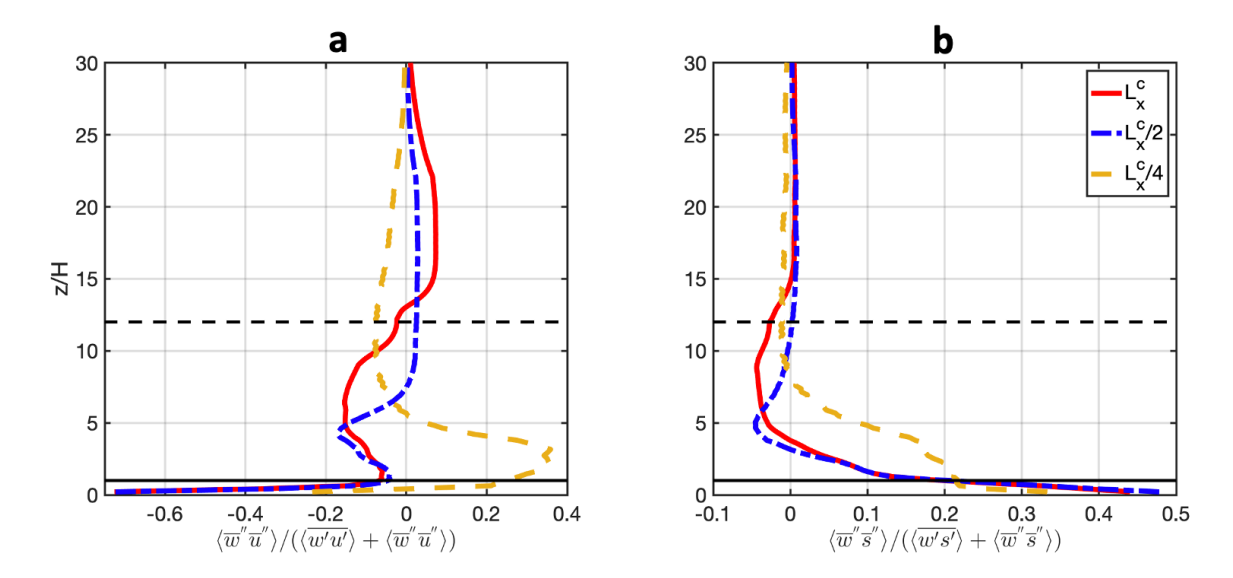


Fig. 13 Normalized dispersive a momentum fluxes **b** scalar fluxes for different averaging scales over the real urban canopy (where L_x^c is the streamwise length of the child domain highlighted by dashed lines in Fig. 6). The dispersive momentum and scalar fluxes are normalized by the sum of their turbulent and dispersive fluxes. Solid horizontal line indicates the mean building height H while the dashed horizontal line is the maximum building height H_{max}

4.2.3 Grid resolution sensitivity

It is a well-known fact that a decrease in grid resolution increases discretization and subgrid-scale model errors when the LES approach is used (Chow and Moin 2003; Meyers et al. 2007). To explore the sensitivity of dispersive fluxes to changes in the grid resolution, we present the profiles of the contribution of dispersive momentum and scalar fluxes to the sum of turbulent and dispersive fluxes at 2 m, 4 m, and 8 m resolutions in Fig. 14. Due to the large computational resources needed for the 2 m resolution simulation, the dispersive fluxes can only be calculated with a smaller temporal averaging interval of 90 T. For consistency, we compare the dispersive fluxes calculated with a temporal averaging interval of 90 T for all grid resolutions. Note that averaging over 90 T suffices to converge the dispersive flux profiles, as shown in Fig. 12. The contribution of dispersive momentum flux and its scalar counterpart vary weakly with the grid resolution (see Fig. 14a,b) especially above H. Below H, the contribution of dispersive momentum flux displays a strong sensitivity to the grid resolution while the contribution of dispersive scalar flux does not. However, the shapes of the profiles and the main conclusions made in previous

sections related to the behaviour of dispersive fluxes above the mean building height are not strongly altered by changing the spatial resolution. We note that the dispersive fluxes presented here are for the entire child domain and thus the findings might not apply to the dispersive fluxes computed over subdomains.

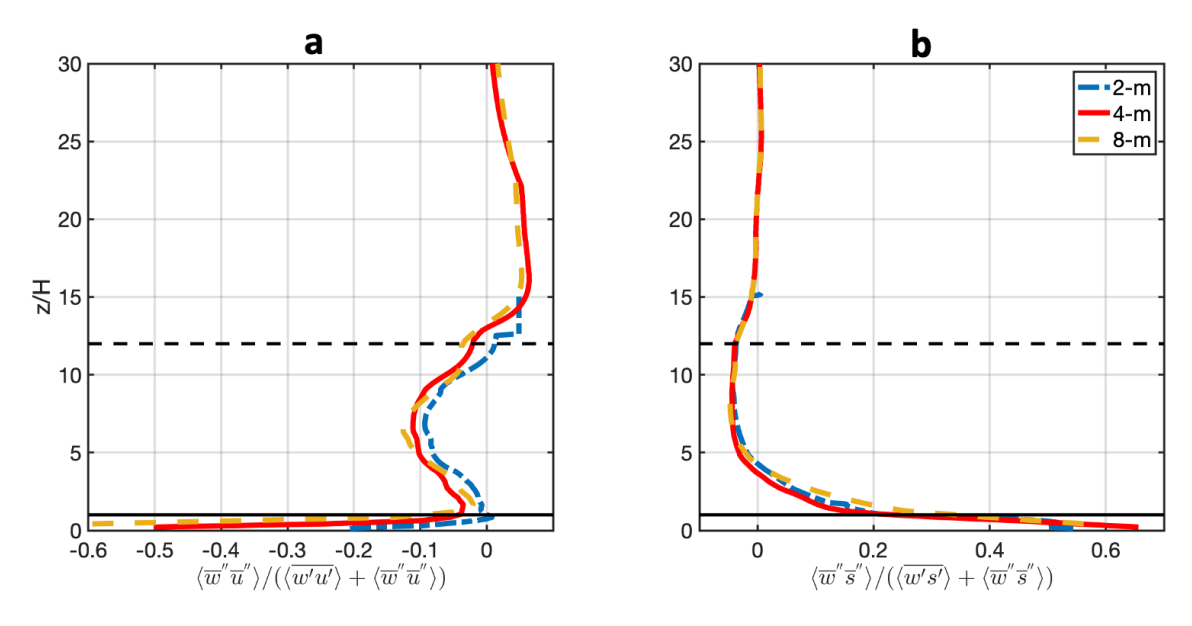


Fig. 14 Normalized dispersive **a** momentum fluxes **b** scalar fluxes for different grid resolutions. The dispersive momentum and scalar fluxes are normalized by the sum of their turbulent and dispersive fluxes. Solid horizontal line indicates the mean building height H while the dashed horizontal line is the maximum building height H_{max} . Temporal averaging was carried out for 90 T for all grid resolutions due to limited computation resources

4.3 Spatial Structure of Dispersive Terms

4.3.1 Spatial Variability of $\overline{w}''\overline{u}''$ and $\overline{w}''\overline{s}''$

In addition to the dispersive fluxes (i.e., spatially averaged $\overline{w}''\overline{u}''$ and $\overline{w}''\overline{s}''$), we examine the spatial variability of $\overline{w}''\overline{u}''$ and $\overline{w}''\overline{s}''$. A direct comparison between $\overline{w'u'}$ and $\overline{w}''\overline{u}''$ at a given x-z plane is presented in Fig. 15. $\overline{w}''\overline{u}''$ spans a broader range of values (about one order of magnitude) than the turbulent momentum flux in the RSL, which agrees with the findings by Giometto et al. (2016). The same is observed for $\overline{w's'}$ and $\overline{w}''\overline{s}''$. These results emphasize the strong spatial heterogeneity of $\overline{w}''\overline{u}''$ and $\overline{w}''\overline{s}''$, and show regions in the RSL where their contributions to the total fluxes can be larger than turbulent fluxes. It is also clear that high-rise buildings enhance the values of $\overline{w}''\overline{u}''$ at higher altitude ($z/H \ge$

3), especially at the leeward side. Negative values of $\overline{w}''\overline{u}''$ are observed at the leeward side of the buildings while positive values are observed at the windward side, especially for regions with high-rise buildings, in agreement with Coceal et al. (2007b) and Blunn et al. (2022). The opposite is seen for $\overline{w}''\overline{s}''$, in which positive values are observed at the leeward side of the buildings while negative values at the windward side (see Fig. 15d). This results from the fact that scalar concentration mostly peaks in low-speed regions.

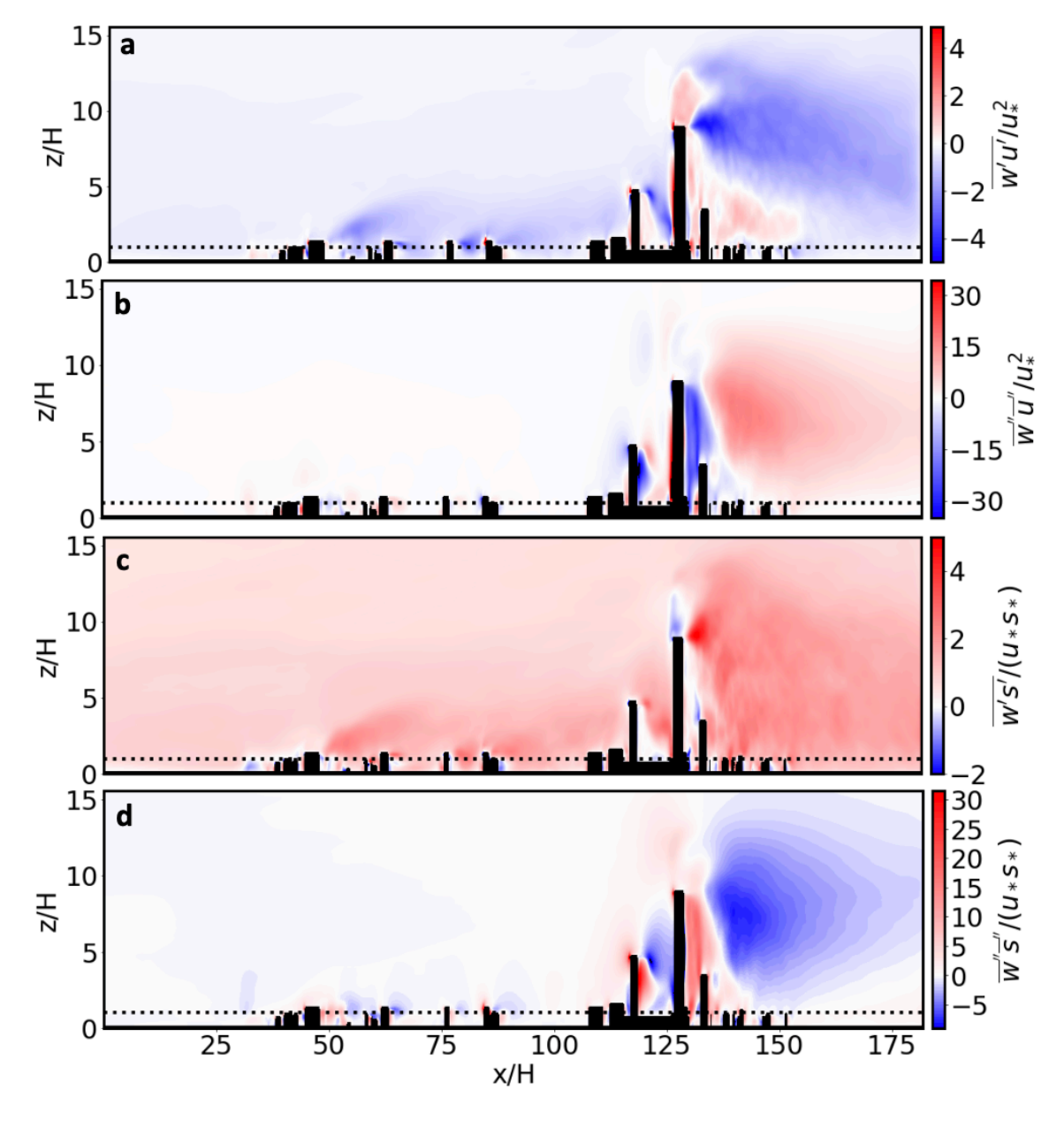


Fig. 15 Colour contour of the spatial variability of dispersive fluxes a $\overline{w'u'}$ b $\overline{w}''\overline{u}''$ c $\overline{w's'}$ d $\overline{w}''\overline{s}''$ at y/H = 116. Momentum fluxes are normalized by the friction velocity u_* while the scalar fluxes are

normalized by u_*s_* . The dashed horizontal line indicates the height z/H=1. The x- axis is defined in terms of the child domain

The standard deviations of $\overline{w}''\overline{u}''$ and $\overline{w}''\overline{s}''$ are presented in Fig. 16. For $\overline{w}''\overline{u}''$, the maximum standard deviation occurs at H. It increases drastically with increase in height to a peak value of 2.35 u_*^2 from the surface and gradually decreases to zero at z/H=15. The standard deviation of $\overline{w}''\overline{s}''$ exhibits a similar profile as $\overline{w}''\overline{u}''$ but has a peak value of 8.41 u_*s_* . In general, $\overline{w}''\overline{u}''$ and $\overline{w}''\overline{s}''$ are spatially heterogeneous within the urban RSL and are clearly enhanced by the presence of high-rise buildings at higher altitude.

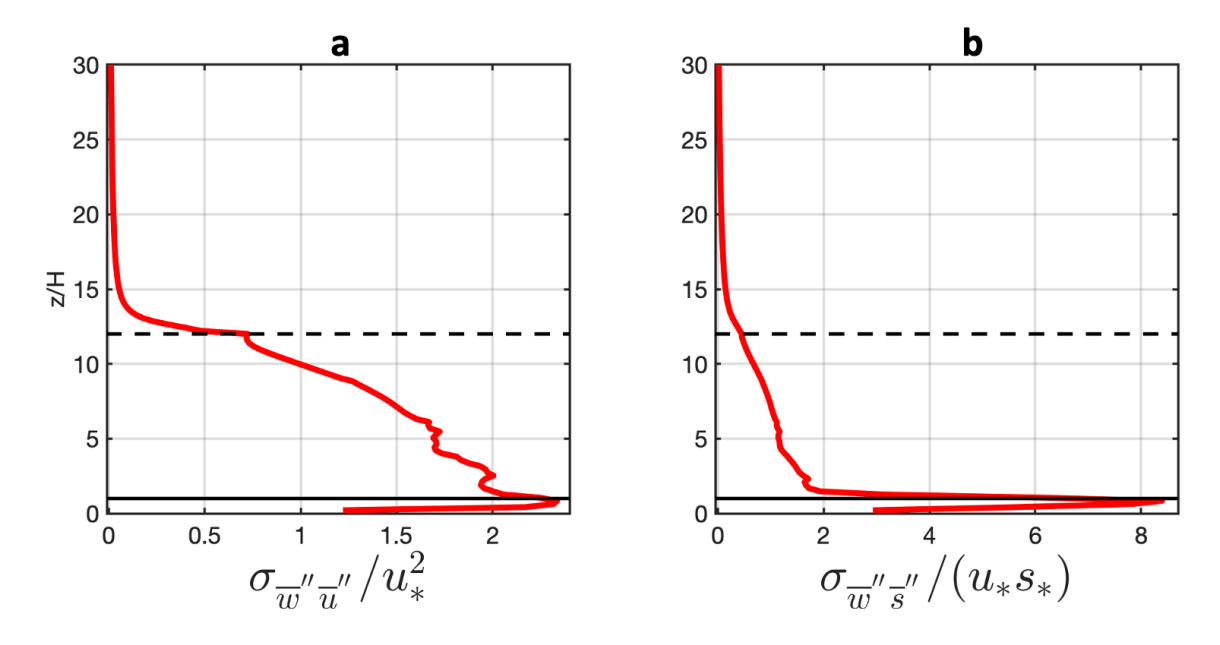


Fig. 16 Standard deviations of $\mathbf{a} \ \overline{w}'' \overline{u}''$ normalized by the friction velocity $u_* \mathbf{b} \ \overline{w}'' \overline{s}''$ normalized by $u_* s_*$. The solid horizontal line indicates the mean building height H while the dashed horizontal line is the maximum building height H_{max} .

4.3.2 Quadrant Analysis

Quadrant analysis is used to quantify the spatial structure of $\overline{w}''\overline{u}''$ and $\overline{w}''\overline{s}''$. Figure 17 shows the quadrant map for $\overline{w}''\overline{u}''$ and $\overline{w}''\overline{s}''$ with color bar showing ejection (E), inward interaction (I), sweep (S) and outward interaction (O). Each grid point in the map corresponds to one of the quadrants based on their definition in Sect. 2.3 (also presented in the caption of Fig. 17). At the interface between the smooth surface and the rough urban

canopy, the dominant quadrant is outward interaction ($\bar{w}'' > 0$ and $\bar{u}'' > 0$) at z/H < 10while the upper part of this interface (i.e., z/H > 10) is dominated by ejection ($\overline{w}'' > 0$ and $\bar{u}'' < 0$). Within the urban canopy, all the quadrants are present but the dominant one is ejection below z/H = 15 while sweep ($\overline{w}'' < 0$ and $\overline{u}'' < 0$) is dominant at $z/H \ge 20$ (not shown). This is also observed in plant-like canopies (Nepf and Koch 1999; Poggi and Katul 2008). The positive \overline{w}'' within the urban canopy and near the ground may be due to the negative pressure gradients introduced by the buildings (Nepf and Koch 1999). At the leeward side of the canopy, the inward interaction is dominant below z/H = 12 as result of negative \overline{w}'' and \overline{u}'' . However, in Poggi and Katul (2008), this quadrant was dominant near the top of the rod forming a vertical secondary circulation with the positive \overline{w}'' near the ground. The variability of the building height in real urban canopy may have prevented the formation of such vertical secondary circulations at lower altitudes. The quadrant map for $\overline{w}''\overline{s}''$ is similar to that for $\overline{w}''\overline{u}''$, except that the vertical extent of the outward interaction $(\overline{w}'' > 0)$ and $\overline{s}'' < 0)$ at the interface between the smooth surface and rough urban surface extends higher than that in $\overline{w}''\overline{u}''$. The dominant quadrant within the urban canopy is also ejection ($\overline{w}'' > 0$ and $\overline{s}'' > 0$). Sweep ($\overline{w}'' < 0$ and $\overline{s}'' < 0$) is the dominant quadrant at the leeward end of the canopy for z/H < 5 while the inward interaction ($\overline{w}'' < 0$ and $\overline{s}'' > 0$) is dominant for z/H > 5.

749

750

751

752

753

754

755

756

757

758

759

760

761

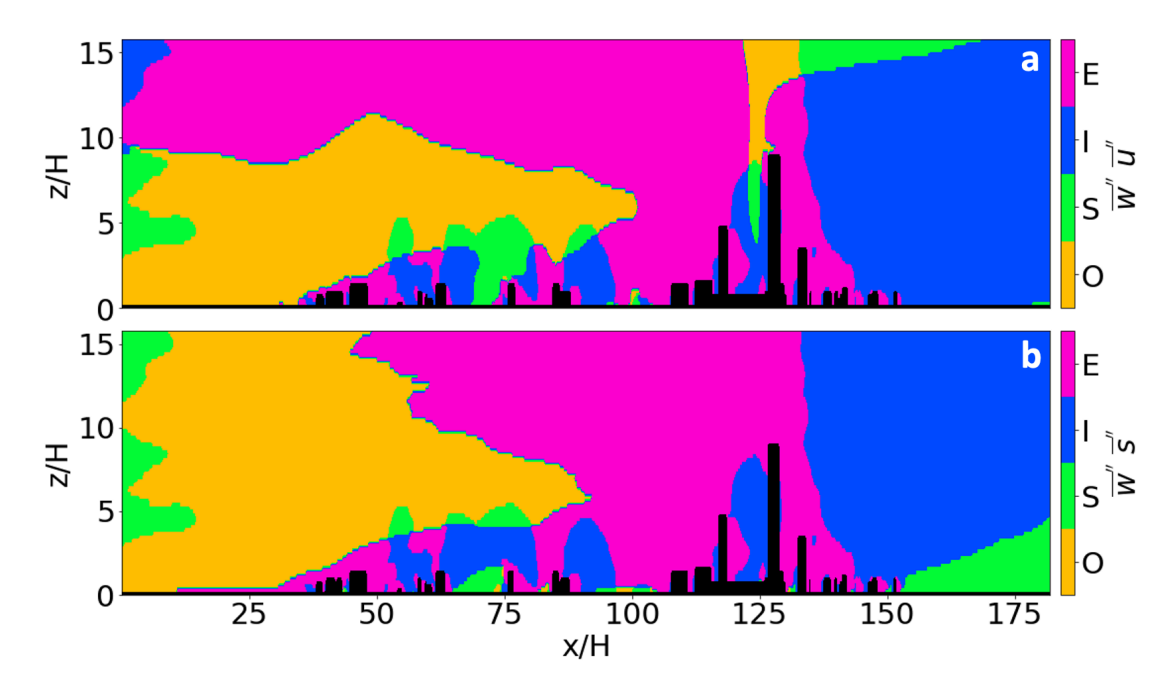
762

763

764

765

766



- Fig. 17 Quadrant map for $\mathbf{a} \ \overline{w}'' \overline{u}''$, and $\mathbf{b} \ \overline{w}'' \overline{s}''$ showing Ejection E ($\overline{w}'' > 0$, $\overline{u}'' < 0$ or $\overline{s}'' > 0$), Inward
- 768 interaction I ($\overline{w}'' < 0$, $\overline{u}'' < 0$ or $\overline{s}'' > 0$), Sweep S ($\overline{w}'' < 0$, $\overline{u}'' > 0$ or $\overline{s}'' < 0$) and Outward interaction
- 769 O $(\overline{w}'' > 0, \overline{u}'' > 0 \text{ or } \overline{s}'' < 0)$ persistent structures at y/H = 116. The x- axis are defined in terms of
- 770 the child domain
- The quadrant map in Fig. 17 only gives information about the quadrant to which each
- point in space belongs. In comparison, the absolute value of the dispersive flux fraction
- 773 F_{i,T_h} normalized by $\sum_i |F_{i,T_h}|$ (hereafter the magnitude of dispersive flux fraction) and the
- corresponding space fraction for different thresholds T_h are presented in Figs. 18 and 19
- respectively, for $\overline{w}''\overline{u}''$. The results for $\overline{w}''\overline{s}''$ are presented in Appendix.
- The magnitude of dispersive flux fractions decreases with increasing threshold T_h . At
- z/H = 1 and z/H = 4, $|F_{i,6}|$ values decrease to half or less of its value at $T_h = 0$ and only
- 778 $|F_{4,10}|$ values exceeded 0.2, which gives evidence that ejections are the largest structures
- involved in momentum transport at these two heights. At z/H = 12, only $|F_{3.10}|$ values
- exceeded 0.35, which shows that the inward interaction has the largest contribution to
- 781 momentum transport at this height. The dominance of ejection at z/H = 1 and z/H = 4
- and inward interactions at z/H = 12 show that strong negative values of \bar{u}'' are present at
- 783 these heights. In the inertial sublayer (at z/H = 30), both $|F_{2,10}|$ and $|F_{4,10}|$ values exceed
- 784 0.2 for $T_h = 10$. This implies that the ejections (dominant above the interface between the
- smooth surface and the rough urban canopy) and sweeps (dominant above the rough urban
- canopy) are the dominant structures at this height, which is consistent with the previous
- 787 study by Shaw et al. (1983).
- In Fig. 19, the space fraction S_{i,T_h} values also decrease with increasing threshold T_h .
- For $T_h = 0$, 37% of the horizontal plane are occupied by negative regimes ($S_{2,0}$ and $S_{4,0}$)
- at z/H = 1 and z/H = 4 while 63% are dominated by 'counter-gradient' regimes ($S_{1.0}$
- and $S_{3,0}$). Christen and Vogt (2004) showed the quadrant analysis of dispersive fluxes
- within a cork oak plantation. In contrast to our study, they found out that 64% of the area
- contributed to negative dispersive fractions ($S_{2,0}$ and $S_{4,0}$) at z/H = 0.18. The resolution
- of our simulation and the limitations of field measurement prevent any form of comparison.

Much higher above the urban canopy (z/H = 12 and z/H = 30), 68% of the horizontal plane are occupied by negative dispersive fractions $(S_{2,0} \text{ and } S_{4,0})$.

In summary, the urban RSL contains persistent structures in all four quadrants but based on the dispersive flux fraction, ejections and inward interactions dominate within the urban canopy while sweeps and ejections dominate above the urban canopy.

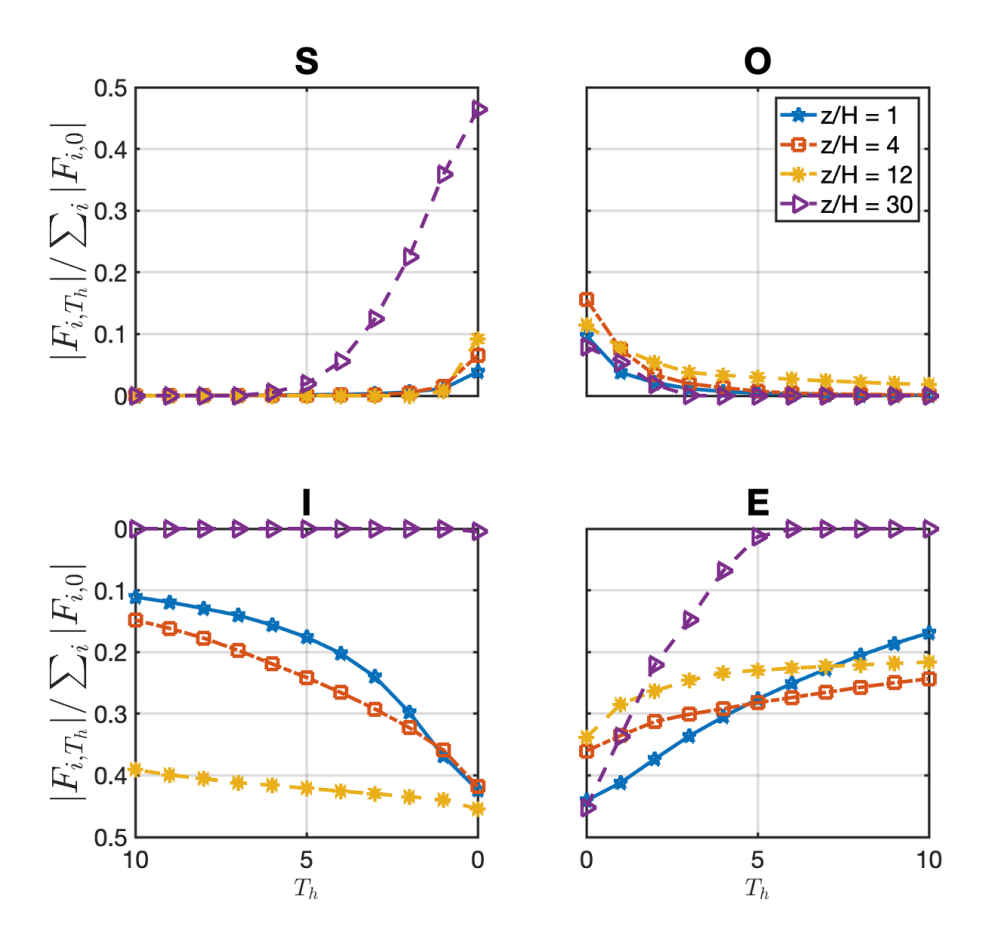


Fig. 18 Absolute value of the dispersive flux fraction F_{i,T_h} normalized by $\sum_i |F_{i,T_h}|$ of each quadrant Q_i to the dispersive flux for different threshold T_h for $\overline{w}''\overline{u}''$. Absolute value of the dispersive flux fraction F_{i,T_h} normalized by $\sum_i |F_{i,T_h}|$ for each quadrant Q_i (Quadrant 1: Outward interaction (O), Quadrant 2: Sweep (S), Quadrant 3: Inward interaction (I), Quadrant 4: Ejection (E)) and for different thresholds T_h for $\overline{w}''\overline{u}''$. The results at heights z/H=1,4,12 and 30 are shown

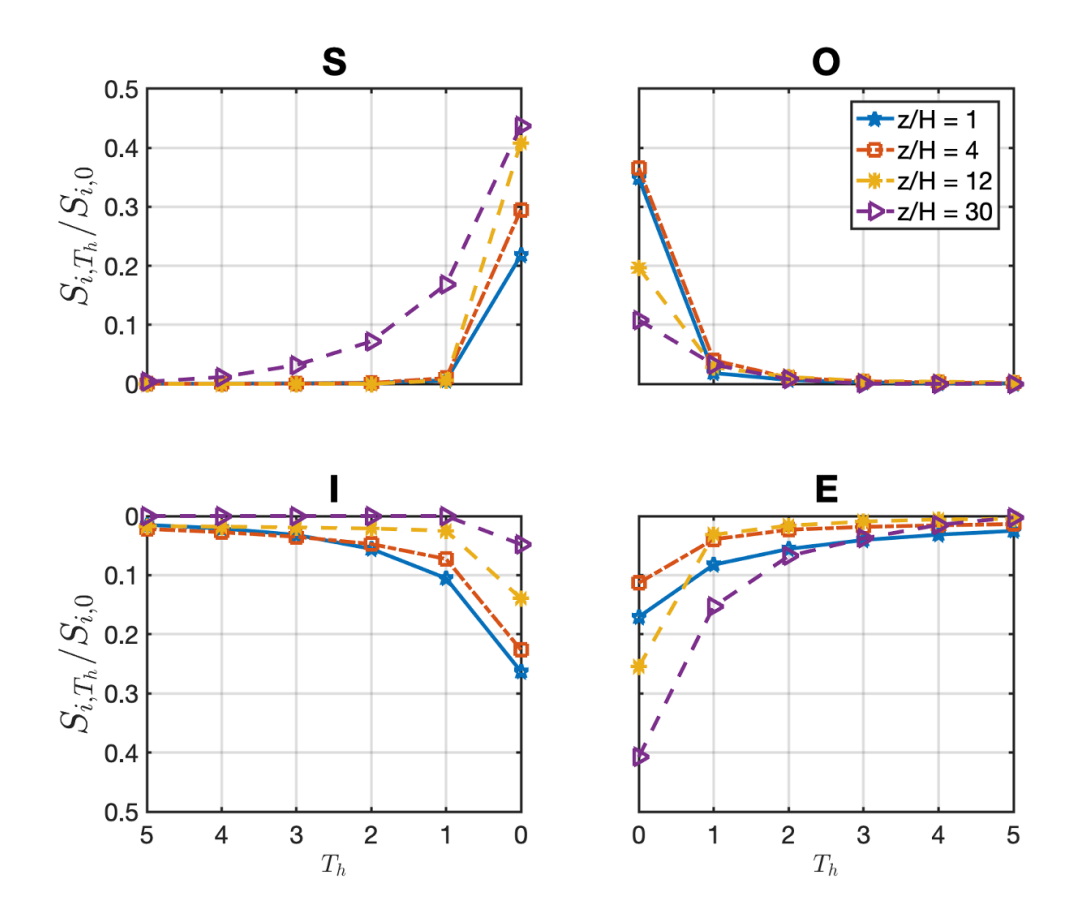


Fig. 19 Space fraction $S_{i,T_h}/S_{i,0}$ for each quadrant Q_i (Quadrant 1: Outward interaction (O), Quadrant 2: Sweep (S), Quadrant 3: Inward interaction (I), Quadrant 4: Ejection (E)) and for different thresholds T_h for $\overline{w}''\overline{u}''$. The results at heights z/H = 1, 4, 12 and 30 are shown

Conclusion

In this study, the transport of momentum and passive scalar over and within a real urban RSL is investigated with the PALM model system in LES mode. The model domain features the Fenway-Kenmore square area in the City of Boston, Massachusetts, USA. The LES model is first evaluated with a simple configuration set up of staggered cubes using previously reported numerical and experimental datasets. We find that the PALM model performs reasonably well in reproducing first- and second-order flow statistics.

The heterogenous nature of the flow, induced by the complex urban canopy, requires the double-averaging procedure to quantify flow statistics. The focus of this study is on dispersive momentum and scalar fluxes, whose importance remains debated. Due to the large variability of building heights in our study domain, the dispersive momentum flux is found to be significant below and above the maximum building height H_{max} with two peak values at z/H = 0.5 and z/H = 5, while the scalar dispersive flux peaks at the mean building height H. The dispersive momentum flux does not become zero until z/H = 30, suggesting a much higher RSL than found in previous studies.

819

820

821

822

823

824

825

826

827

828

829

830

831

832

833

834

835

836

837

838

839

840

841

842

843

844

845

846

847

848

The double-averaging procedure used in the calculation of dispersive fluxes requires temporal and spatial averaging. The sensitivity of the dispersive fluxes in real urban canopies to both averaging is carried out. Previous studies over urban-like canopies reveal the presence of secondary circulations that are triggered by urban roughness. These circulations cause the dispersive fluxes to be large when averages are performed over short time scales and small for long time scales. In this study, statistical convergence is obtained with time averaging of 360 T or 720 T, where T is the eddy turnover time. However, we caution that the time averaging scale needed to reach statistical convergence for dispersive fluxes may depend on the domain size. Also, the dispersive fluxes are sensitive to changes in spatial averaging scale. We find that the peak of the dispersive momentum flux increases as the spatial scale decreases while the dispersive scalar flux slightly decreases with decreases in the spatial scale, but this conclusion may depend on other parameters such as the distance to the transition from non-urban to urban areas and the plan area fractions within the spatial averaging domain. We also test the sensitivity of dispersive fluxes to the grid spacing. Above the mean building height, the sensitivity of dispersive fluxes to the grid spacing is rather weak. However, below the mean building height, the dispersive momentum flux displays a strong dependency on the grid spacing. In general, our main findings related to the behaviour of dispersive fluxes above the mean building height are not influenced by the grid spacing.

We also examine the spatial variability of $\overline{w}''\overline{u}''$ and $\overline{w}''\overline{s}''$, including their standard deviations and spatially persistent structures. The $\overline{w}''\overline{u}''$ and $\overline{w}''\overline{s}''$ show a broader range of values when compared with turbulent fluxes in RSL and are enhanced by the presence of high-rise buildings. The quadrant analysis reveals that ejection and inward interactions are the dominant structures contributing to dispersive momentum transport within the canopy while sweep and ejection are dominant above the canopy.

This study highlights the importance of dispersive fluxes over real urban canopies and thus the need to parameterize both turbulent and dispersive fluxes in mesoscale models.

Our conclusions are based on assuming neutral stratification and future investigations on the effects of stratification (stable or unstable) are needed.

Acknowledgements This research was funded by National Science Foundation (NSF) under the Award number AGS-1853354 and ICER-1854706 and Army Research Office (ARO) under the Award number W911NF-18-1-0360. We acknowledge the high-performance computing support from Cheyenne (doi:10.5065/D6RX99HX) provided by NCAR's Computational and Information Systems Laboratory, sponsored by the National Science Foundation. Finally, we thank the PALM group at the Institute of Meteorology and Climatology of Leibniz Universität Hannover, Germany for their technical support.

Data Availability Statement The datasets generated and analyzed during this study are available from the corresponding author on reasonable request.

Appendix: Dispersive Flux Fraction and Spatial Fraction for $\overline{w}''\overline{s}''$

For $\overline{w}''\overline{s}''$, the magnitude of dispersive flux fraction decreases with height only for ejection (F_{1,T_h}) at all thresholds and decreases with increasing thresholds T_h for all heights, like $\overline{w}''\overline{u}''$ (see Fig. 20). At z/H=1 and z/H=4, only $|F_{1,4}|$ values exceeded 0.25, which is evidence that ejections are the largest structures involved in scalar transport. At z/H=12, only $|F_{4,4}|$ values exceed 0.35 and at z/H=30 only $|F_{4,4}|$ values exceed 0.2, which shows that the outward interaction has the largest contribution to scalar transport at these two heights. The inward interaction $(S_{2,0})$ occupies the largest horizontal plane for all heights

(see Fig. 21). In summary, ejections and outward interactions are the dominant structure within the urban canopy and inertial sublayer respectively, for $\overline{w}''\overline{s}''$.

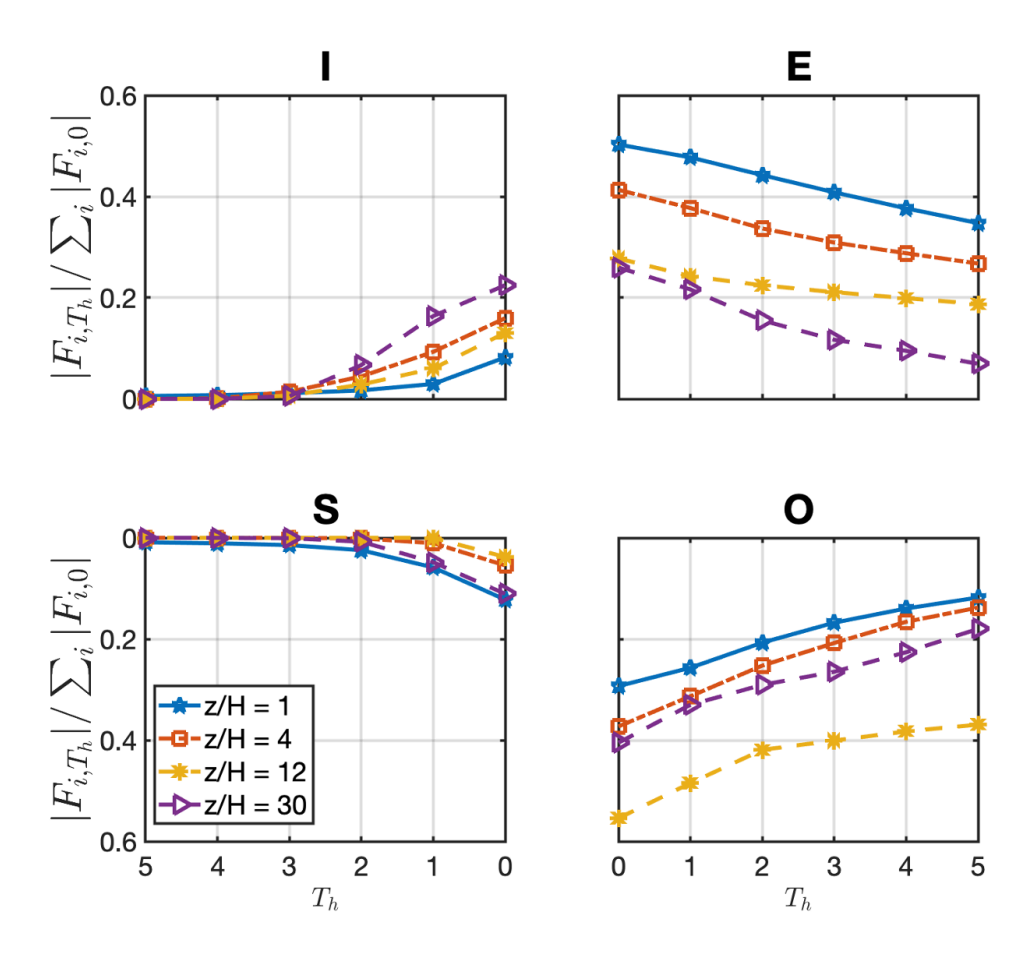


Fig. 20 Absolute value of the dispersive flux fraction F_{i,T_h} normalized by $\sum_i |F_{i,T_h}|$ of quadrant Q_i to the dispersive flux for different threshold T_h for $\overline{w}''\overline{s}''$ showing Ejection E, Inward interaction I, Sweep S and Outward interaction O persistent structures at heights z/H = 1, 4, 12 and 30

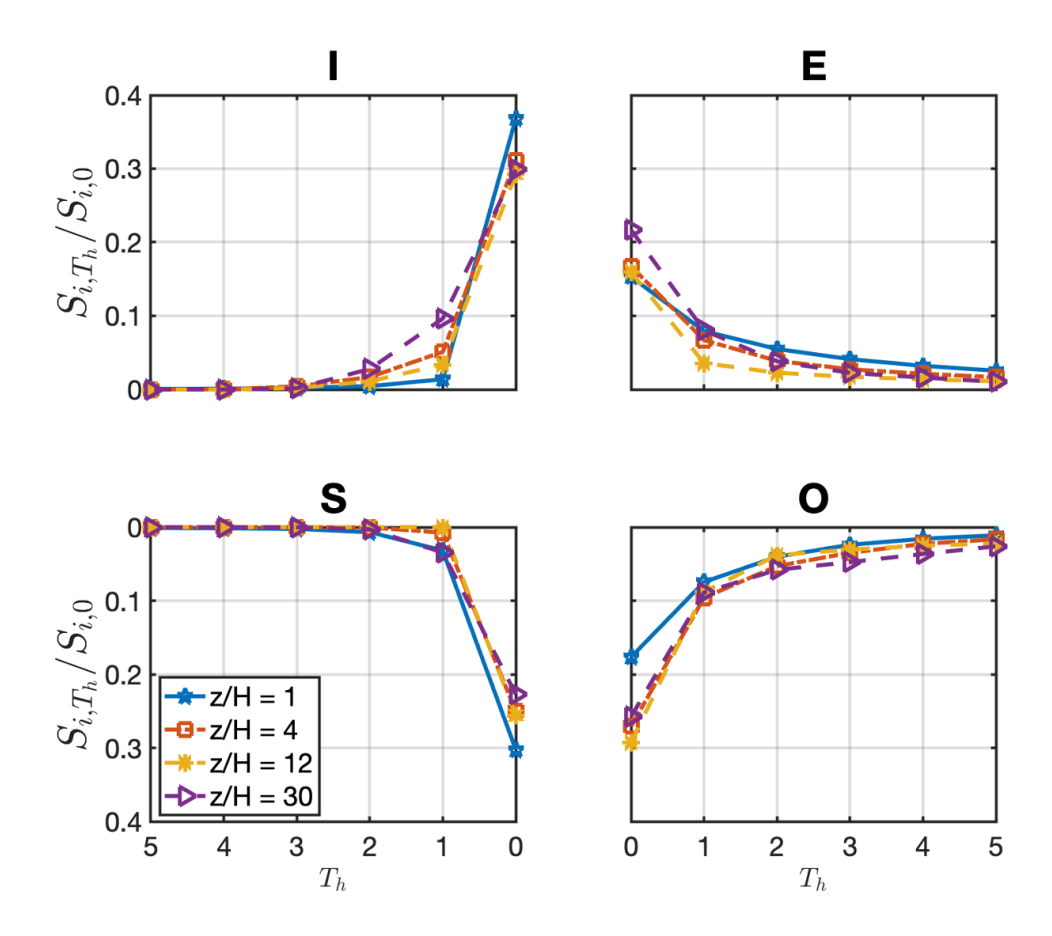


Fig. 21 Spatial fraction $S_{i,T_h}/S_{i,0}$ of quadrant Q_i to the dispersive flux for different threshold T_h for $\overline{w}''\overline{s}''$ showing Ejection E, Inward interaction I, Sweep S and Outward interaction O persistent structures at heights z/H = 1, 4, 12 and 30

References

Evidence from Large-Eddy Simulations. J. Fluid Mech., 789, 567–588

Aristodemou E, Boganegra LM, Mottet L, Pavlidis D, Constantinou A, Pain C, Robins A, ApSimon H (2018)
How tall buildings affect turbulent air flows and dispersion of pollution within a neighbourhood.
Environ. Pollut. 233, 782-796

Auvinen M, Boi S, Hellsten A, Tanhuanpää T, Järvi L (2020) Study of Realistic Urban Boundary Layer
Turbulence with High-Resolution Large-Eddy Simulation. Atmosphere, 11, 201

Avissar R, Chen F (1993) Development and analysis of prognostic equations for mesoscale kinetic energy
and mesoscale (subgrid scale) fluxes for large-scale atmospheric models. J. Atmos. Sci., 50(22), 3751-

Anderson W (2016) Amplitude Modulation of Streamwise Velocity Fluctuations in the Roughness Sublayer:

888 Bailey BN, Stoll R (2013) Turbulence in Sparse, Organized Vegetative Canopies: A Large-Eddy Simulation 889 Study. Boundary-Layer Meteorol. 147, 369-400 890 Balakumar BJ, Adrian RJ (2007) Large- and very-large-scale motions in channel and boundary-layer flows, 891 Phil. Trans. R. Soc. A.365665-681 892 Basu S, Lacser A (2017) A Cautionary Note on the Use of Monin-Obukhov Similarity Theory in Very High-893 Resolution Large-Eddy Simulations. Boundary-Layer Meteorol 163, 351–355 894 Belcher SE, Jerram N, Hunt JCR (2003) Adjustment of a turbulent boundary layer to a canopy of roughness 895 elements. J. Fluid Mech. 488, 369-398 896 Blackman K, Perret L (2016) Non-linear interactions in a boundary layer developing over an array of cubes 897 using stochastic estimation. Phys. Fluids 28(9), 095-108 898 Blackman K, Perret L, Calmet I, Rivet C (2017) Turbulent kinetic energy budget in the boundary layer 899 developing over an urban-like rough wall using PIV, Phys. Fluids 29, 085113 900 Blunn LP, Coceal O, Nazarian N, Barlow JF, Plant RS, Bohnenstengel SI, Lean HW (2022) Turbulence 901 Characteristics Across a Range of Idealized Urban Canopy Geometries. Boundary-Layer Meteorol. 182, 902 275-307 903 Bohm M, Finnigan JJ, Raupach MR (2000) Dispersive Fluxes and Canopy Flows: Just How Important Are 904 They? American Meteorology Society, 24th Conference on Agricultural and Forest Meteorology, 905 University of California, Davis, CA, pp. 106–107 906 Böhm M, Finnigan JJ, Raupach MR, Hughes D (2013) Turbulence Structure Within and Above a Canopy of 907 Bluff Elements. Boundary-Layer Meteorol. 146, 393-419 908 Bou-Zeid E, Overney J, Rogers BD, Parlange MB (2009) The Effects of Building Representation and 909 Clustering in Large-Eddy Simulations of Flows in Urban Canopies. Boundary-Layer Meteorol 132, 415– 910 436 911 Briscolini M, Santangelo P (1989) Development of the mask method for incompressible unsteady flows, J. 912 Comput. Phys., 84(1), 57-75 913 Britter RE, Hunt JCR (1979) Velocity measurements and order of magnitude estimates of the flow between 914 two buildings in a simulated atmospheric boundary layer. J. Indust. Aerodyn. 4, 165-182 915 Britter RE, Hanna SR (2003) Flow and dispersion in urban areas. Annu Rev Fluid Mech 35(1): 469-496 916 Buccolieri R, Hang J (2019) Recent Advances in Urban Ventilation Assessment and Flow 917 Modelling. Atmosphere 10, 144

918 919 920	heterogeneities, dispersive fluxes and the conundrum of unaccounted statistical spatial inhomogeneities, EGU General Assembly 2020, Online, 4–8 May 2020, EGU2020-13388
921 922	Castro IP, Cheng H, Reynolds R (2006) Turbulence over urban-type roughness: deductions from wind tunnel measurements. Boundary-Layer Meteorol. 118, 109–131
923 924	Chen F, Avissar R (1994) The impact of land-surface wetness heterogeneity on mesoscale heat fluxes. J. App. Meteorol. Climatol., 33(11), 1323-1340
925 926	Cheng H, Castro IP (2002) Near Wall Flow Over Urban-like Roughness. Boundary-Layer Meteorol. 104, 229–259
927 928	Cheng H, Hayden P, Robins AG, Castro IP (2007) Flow over cube arrays of different packing densities. J. Wind Engin. Ind. Aerodyn. 95 (8), 715–740
929 930 931	Cheng WC, Liu CH, Ho YK, Mo Z, Wu Z, Li W, Chan LYL, Kwan WK, Yau HT (2021) Turbulent flows over real heterogeneous urban surfaces: Wind tunnel experiments and Reynolds-averaged Navier-Stokes simulations. Build. Simul., 14, 1345-1358
932 933	Chow FK, Moin P (2003) A further study of numerical errors in large eddy simulations. J. Comput. Phys., 184(2) 366-380
934 935	Christen A, van Gorsel E, Vogt R (2007) Coherent structures in urban roughness sublayer turbulence. Int J Climatol 27(14):1955-1968
936 937 938	Christen A, Vogt R (2004) Direct measurement of dispersive fluxes within a Cork Oak plantation. 26th AMS conference on agricultural and forest meteorology, American Meteorological Society, Vancouver, BC, pp 86
939 940	Christen A, Rotach MW, Vogt R (2009) The budget of turbulent kinetic energy in the urban roughness sublayer. Boundary-Layer Meteorol 131(2):193-222
941 942	Chung D, McKeon BJ (2010) Large-Eddy Simulation of Large-Scale Structures in Long Channel Flow. J. Fluid Mech., 661, 341–364
943 944	Coceal O, Thomas TG, Castro IP, Belcher SE (2006) Mean flow and turbulence statistics over groups of urban-like cubical obstacles. Boundary-Layer Meteorol. 121, 491–519
945 946	Coceal O, Dobre A, Thomas T, Belcher S (2007a) Structure of turbulent flow over regular arrays of cubical roughness. J. Fluid Mech., 589, 375-409
947 948	Coceal O, Thomas TG, Belcher SE (2007b) Spatial Variability of Flow Statistics within Regular Building Arrays. Boundary-Layer Meteorol. 125, 537–552

949 Efthimiou GC, Andronopoulos S, Bartzis JG, Berbekar E, Harms F, Leitl B (2017) CFD-RANS prediction 950 of individual exposure from continuous release of hazardous airborne materials in complex urban 951 environments, J Turbul., 18:2, 115-137 952 Eliasson I, Offerle B, Grimmond CSB, Lindqvist S (2006) Wind fields and turbulence statistics in an urban 953 street canyon. Atmospheric Environ 40(1): 1-16 954 Fang J, Porté-Agel F (2015) Large-Eddy Simulation of Very-Large-Scale Motions in the Neutrally 955 Stratified Atmospheric Boundary Layer. Boundary-Layer Meteorol 155, 397-416 956 Fernando HJS, Lee SM, Anderson J, Princevac M, Pardyjak E, Grossman-Clarke S (2001) Urban fluid 957 mechanics: Air circulation and contaminant dispersion in cities, Environ. Fluid Mech. 1, 107 958 Fernando HJS, Zajic D, Di Sabatino S, Dimitrova R, Hedquist B, Dallman A (2010) Flow, turbulence, and 959 pollutant dispersion in urban atmospheres, Phys. Fluids 22, 051301 960 Finnigan J (2000) Turbulence in plant canopies. Ann. Rev. Fluid Mech., 32:1, 519 – 571 961 Fishpool GM, Lardeau S, Leschziner MA (2009) Persistent Non-Homogeneous Features in Periodic 962 Channel-Flow Simulations. Flow Turbul Combust 83, 323-342 963 Flaherty JE, Stock D, Lamb B (2007) Computational fluid dynamic simulations of plume dispersion in urban 964 Oklahoma City. J. Appl Meteorol and Climatol., 46: 2110-2126 965 Fröhlich D, Matzarakis A (2020) Calculating human thermal comfort and thermal stress in the PALM model 966 system 6.0, Geosci. Model Dev., 13, 3055-3065 967 Giometto MG, Christen A, Meneveau C, Fang J, Krafczyk M, Parlange MB (2016) Spatial characteristics of 968 roughness sublayer mean flow and turbulence over a realistic urban surface. Boundary-Layer 969 Meteorol. 160(3), 425–452 970 Giometto MG, Christen A, Egli PE, Schmid MF, Tooke RT, Coops NC, Parlange MB (2017) Effects of trees 971 on mean wind, turbulence, and momentum exchange within and above a real urban environment. Adv. 972 Water 106, 154-168 973 Grimmond CSB, Oke TR (1999) Aerodynamic properties of urban areas derived from analysis of surface 974 form. J Appl Meteorol 38(9): 1262-1292 975 Gronemeier T Raasch S, Ng E (2017) Effects of Unstable Stratification on Ventilation in Hong Kong. 976 Atmosphere., 8 (9), 168 977 Gronemeier T, Suhring M (2019) On the Effects of Lateral Openings on Courtyard Ventilation and Pollution, 978 A Large-Eddy Simulation Study. Atmosphere 10(2), 63 979 Gronemeier T, Surm K, Harms F, Leitl B, Maronga B, Raasch S (2021) Evaluation of the dynamic core of 980 the PALM model system 6.0 in a neutrally stratified urban environment: comparison between LES and 981 wind-tunnel experiments, Geosci. Model Dev., 14, 3317–3333

982 Hackbusch W (1985) Multigrid Methods and Applications. Springer. Berlin, Heidelberg, New York, pp. 378 983 Hellsten A, Ketelsen K, Sühring M, Auvinen M, Maronga B, Knigge C, Barmpas F, Tsegas G, 984 Moussiopoulos N, Raasch S (2021) A nested multi-scale system implemented in the large-eddy 985 simulation model PALM model system 6.0, Geosci. Model Dev., 14, 3185-3214 986 Herpin S, Perret L, Mathis R, Tanguy C, Lasserre JJ (2018) Investigation of the flow inside an urban canopy 987 immersed into an atmospheric boundary layer using laser Doppler anemometry. Exp Fluids 59, 80 988 Hertwig D, Gough HL, Grimmond S, Barlow JF, Kent CW, Lin WE, Robins AG, Hayden P (2019) Wake 989 Characteristics of Tall Buildings in a Realistic Urban Canopy, Boundary-Layer Meteorol 172, 239-270 990 Hutchins N, Marusic I (2007) Evidence of very long meandering features in the logarithmic region of 991 turbulent boundary layers. J. Fluid Mech., 579, 1–28 992 Hutchins N, Chauhan K, Marusic I, Monty J, Klewicki J (2012) Towards Reconciling the Large-Scale 993 Structure of Turbulent Boundary Layers in the Atmosphere and Laboratory. Boundary-Layer 994 Meteorol. 145, 273-306 995 Inagaki A, Castillo MCL, Yamashita Y, Kanda M, Takimoto H (2012) Large-Eddy Simulation of Coherent 996 Flow Structures within a Cubical Canopy. Boundary-Layer Meteorol 142, 207–222 997 Inagaki A, Kanda M, Ahmad NH, Yagi A, Onodera N, Aoki T (2017) A Numerical Study of Turbulence 998 Statistics and the Structure of a Spatially Developing Boundary Layer Over a Realistic Urban Geometry. 999 Boundary-Layer Meteorol 164, 161-181 1000 Jimenez J (2004) Turbulent flows over rough walls. Annu Rev Fluid Mech. 36(1):173-196 1001 Kaimal JC, Finnigan JJ (1994) Atmospheric Boundary Layer Flows: Their Structure and Measurement, 1002 Oxford University Press, pp. 289 1003 Kanda M (2006) Large-eddy simulations on the effects of surface geometry of building arrays on turbulent 1004 organized structures. Boundary-Layer Meteorol. 118, 151-168 1005 Kanda M, Inagaki A, Miyamoto T, Gryschka M, Raasch S (2013) A New Aerodynamic Parametrization for 1006 Real Urban Surfaces. Boundary-Layer Meteorol 148, 357–377 1007 Karttunen S, Kurppa M, Auvinen M, Hellsten A, Järvi L (2020) Large-eddy simulation of the optimal street-1008 tree layout for pedestrian-level aerosol particle concentrations - A case study from a city-1009 boulevard. Atmospheric Environ., X 6, 100073 1010 Kataoka H, Mizuno M (2002) Numerical flow computation around aerolastic 3D square cylinder using inflow 1011 turbulence. Wind Struct. 5: 379-392 1012 Katul G, Kuhn G, Schieldge J., Hsieh C-I (1997) The ejection-sweep character of scalar fluxes in the unstable 1013 surface layer. Boundary-Layer Meteorol. 83, 1-26

1014 1015 1016	Kurppa M, Roldin P, Strömberg J, Balling A, Karttunen S, Kuuluvainen H, Niemi JV, Pirjola L, Rönkkö T Timonen H, Hellsten A, Järvi L (2020) Sensitivity of spatial aerosol particle distributions to the boundary conditions in the PALM model system 6.0, Geosci. Model Dev., 13, 5663–5685
1017 1018	Leonardi S, Orlandi P, Djenidi L, Antonia RA (2015) Heat transfer in a turbulent channel flow with square bars or circular rods on one wall. J. Fluid Mech., 776, 512–530
1019 1020	Letzel MO, Krane M, Raasch S (2008) High resolution urban large-eddy simulation studies from street canyon to neighbourhood scale. Atmospheric Environ. 42, 8770-8784
1021 1022	Li D, Bou-Zeid E (2011) Coherent structures and the dissimilarity of turbulent transport of momentum and scalars in the unstable atmospheric surface layer, Boundary-Layer Meteorol., 140(2), 243-262
1023 1024	Li Q, Bou-Zeid E (2019) Contrasts between momentum and scalar transport over very rough surfaces. J Fluid Mech. 880:32–58
1025 1026	Lund TS, Wu X, Squires KD (1998) Generation of turbulent inflow data for spatially developing boundary layer simulations. J. Comput. Phys. 140: 233–258
1027	Mahrt L (1987) Grid-averaged surface fluxes. Mon. Weather Rev., 115(8), 1550-1560
1028 1029	Mahrt L (2010) Computing turbulent fluxes near the surface: needed improvements. Agric. For. Meteorol. 150(4), 501-509
1030 1031 1032 1033	Makedonas A, Carpentieri M, Placidi M (2021) Urban Boundary Layers Over Dense and Tall Canopies. Boundary-Layer Meteorol 181, 73–93 Maronga B, Raasch S (2013) Large-Eddy Simulations of Surface Heterogeneity Effects on the Convective Boundary Layer During the LITFASS-2003 Experiment. Boundary-Layer Meteorol 146, 17–44
1034 1035 1036 1037	Maronga B, Gryschka M, Heinze R, Hoffmann F, Kanani-Sühring F, Keck M, Ketelsen K, Letzel MO Sühring M, Raasch S (2015) The Parallelized Large-Eddy Simulation Model (PALM) version 4.0 for atmospheric and oceanic flows: model formulation, recent developments, and future perspectives Geosci. Model Dev., 8, 1539-1637
1038 1039 1040 1041 1042 1043	Maronga B, Banzhaf S, Burmeister C, Esch T, Forkel R, Fröhlich D, Fuka V, Gehrke KF, Geletič J, Giersch S, Gronemeier T, Groß G, Heldens W, Hellsten A, Hoffmann F, Inagaki A, Kadasch E, Kanani-Sühring F, Ketelsen K, Khan BA, Knigge C, Knoop H, Krč P, Kurppa M, Maamari H, Matzarakis A, Mauder M Pallasch M, Pavlik D, Pfafferott J, Resler J, Rissmann S, Russo E, Salim M, Schrempf M, Schwenkel J Seckmeyer G, Schubert S, Sühring M, von Tils R, Vollmer L, Ward S, Witha B, Wurps H, Zeidler J Raasch S (2020) Overview of the PALM model system 6.0, Geosci. Model Dev., 13, 1335–1372
1044 1045	Mason, P (1995) Atmospheric boundary layer flows: Their structure and measurement. Boundary-Layer Meteorol 72, 213–214

1046 Mathis R, Hutchins N, Marusic I (2009) Large-scale amplitude modulation of the small-scale structures in 1047 turbulent boundary layers, J. Fluid Mech., 628, 311–337 1048 Meyers J, Geurts BJ, Sagaut P (2007) A computational error assessment of central finite-volume 1049 discretizations in large-eddy simulation using a Smagorinsky model. J. Comput. Phys., 227(1), 156 – 1050 173 1051 Mignot E, Barthelemy E, Hurther D (2009) Double-Averaging Analysis and Local Flow Characterization of 1052 near-Bed Turbulence in Gravel-Bed Channel Flows. J. Fluid Mech., 618, 279-303 1053 Mo ZW, Liu CH, Ho YK (2021) Roughness sublayer flows over real urban morphology: A wind-tunnel 1054 study. Build Environ. 188, 107463 1055 Moltchanov S, Bohbot-Raviv Y, Duman T, Shavit U (2015) Canopy edge flow: a momentum balance 1056 analysis. Water Resour Res 51(4):2081-2095 1057 Monin AS, Obukhov AM (1954) Basic laws of turbulent mixing in the surface layer of the atmosphere. Tr. 1058 Akad. Nauk. SSSR Geophiz. Inst. 24 (151): 163 - 187 1059 Nazarian N, Krayenhoff ES, Martilli A (2020) A one-dimensional model of turbulent flow through "urban" 1060 canopies (MLUCM v2.0): updates based on large-eddy simulation, Geosci. Model Dev., 13, 937–953 Nepf HM, Koch EW (1999) Vertical secondary flows in submersed plant-like arrays, Limnol 1061 1062 Oceanogr., 44(4), 1072-1080 1063 Nikora V, McLean S, Coleman S, Pokrajac D, McEwan I, Campbell L, Aberle J, Clunie D, Koll K (2007) 1064 Double-averaging concept for rough-bed open-channel and overland flows: theoretical background. J 1065 Hydraul. Eng. 133(8):884-895 1066 Niroobakhsh A, Hassanzadeh S, Hosseinibalam F (2022) The vital importance of dispersive fluxes on 1067 turbulent flow and pollution ventilation in street canyons. Urban Clim. 41, 101032 1068 Obukhov AM (1971) Turbulence in an atmosphere with a non-uniform temperature. Boundary-Layer 1069 Meteorol. 2, 7-29 1070 Oke TR (1988) Street design and urban canopy layer climate. Energy and Buildings. 11 (1–3): 103–113 1071 Oke TR, Mills G, Christen A, Voogt J (2017) Urban Climates. Cambridge University Press. 1072 Park SB, Baik JJ, Raasch S, Letzel MO (2012) A Large-Eddy Simulation Study of Thermal Effects on 1073 Turbulent Flow and Dispersion in and above a Street Canyon. J. Appl. Meteorol Clim. 51, 829-841 1074 Park SB, Baik JJ, Han BS (2015) Large-eddy simulation of turbulent flow in a densely built-up urban area. 1075 Environ Fluid Mech 15, 235-250 1076 Poggi D, Katul GG, Albertson JD (2004) A Note on The Contribution of Dispersive Fluxes to Momentum 1077 Transfer Within Canopies. Boundary-Layer Meteorol. 111, 615–621

1078	Poggi D, Katul GG (2008) The effect of canopy roughness density on the constitutive components of the dispersive stresses. Exp Fluids 45, 111–121
1080 1081	Pokrajac D, Campbell LJ, Nikora V, Manes C, McEwan I (2007) Quadrant analysis of persistent spatial velocity perturbations over square-bar roughness. Exp Fluids 42, 413–423
1082 1083	Ramamurthy P, Pardyjak ER, Klewicki JC (2007) Observations of the effects of atmospheric stability on turbulence statistics deep within an urban street canyon. J Appl Meteorol Climatol 46(12):2074-2085
1084 1085	Ramamurthy P, Pardyjak ER (2015) Turbulent transport of carbon dioxide over a highly vegetated suburban neighbourhood. Boundary-Layer Meteorol 157(3):461 - 479
1086 1087	Rasheed A, Robinson D (2013) Characterization of Dispersive Fluxes in Mesoscale Models Using LES of Flow over an Array of Cubes, Int. J. Atmos. Sci., 10, 898095
1088 1089	Raupach MR (1981) Conditional statistics of Reynolds stress in rough-wall and smooth-wall turbulent boundary layers. J Fluid Mech 108:363–382
1090 1091	Raupach MR, Shaw RH (1982) Averaging procedures for flow within vegetation canopies. Boundary-Layer Meteorol 22, 79-90
1092 1093	Raupach MR, Coppin PA, Legg BJ (1986) Experiments on scalar dispersion within a model plant canopy part I: The turbulence structure. Boundary-Layer Meteorol. 35, 21–52
1094 1095	Raupach MR, Antonia RA, Rajagopalan S (1991) Rough-Wall Turbulent Boundary Layers. ASME. Appl. Mech. Rev 44(1): 1–25
1096 1097	Raupach MR (1994) Simplified expressions for vegetation roughness length and zero-plane displacement as functions of canopy height and area index. Boundary-Layer Meteorol 71, 211–216
1098 1099	Raupach MR, Finnigan JJ, Brunei Y (1996) Coherent eddies and turbulence in vegetation canopies: The mixing-layer analogy. Boundary-Layer Meteorol. 78, 351–382
1100 1101 1102 1103	Resler J, Eben K, Geletič J, Krč P, Rosecký M, Sühring M, Belda M, Fuka V, Halenka T, Huszár P, Karlický J, Benešová N, Ďoubalová J, Honzáková K, Keder J, Nápravníková Š, Vlček O (2021) Validation of the PALM model system 6.0 in a real urban environment: a case study in Dejvice, Prague, the Czech Republic, Geosci. Model Dev., 14, 4797–4842
1104 1105	Rotach MW (1999) On the influence of the urban roughness sublayer on turbulence and dispersion. Atmos. Environ 33(24):4001-4008
1106	Roth M (2000) Review of atmospheric turbulence over cities. Q J R Meteorol Soc 126(564):941 – 990
1107 1108	Scarano F, Riethmuller ML (2000) Advances in iterative multigrid PIV image processing. Exp. Fluids 29(1): S051–S060

- Schmid MF, Lawrence GA, Parlange MB, Giometto MG (2019) Volume Averaging for Urban Canopies.
 Boundary-Layer Meteorol 173, 349-372
- Shaw RH, Tavangar J, Ward DP (1983) Structure of Reynolds stress in a canopy layer. J Clim Appl Meteorol.
- 1112 22:1922–1931
- 1113 Sützl BS, Rooney GG, van Reeuwijk M (2021) Drag Distribution in Idealized Heterogeneous Urban
- Environments. Boundary-Layer Meteorol 178, 225–248
- 1115 Tian G, Conan B, Calmet I (2021) Turbulence-Kinetic-Energy Budget in the Urban-Like Boundary Layer
- 1116 Using Large-Eddy Simulation. Boundary-Layer Meteorol 178, 201–223
- 1117 Tominaga Y, Stathopoulos T (2013) CFD simulation of near-field pollutant dispersion in the urban
- environment: A review of current modeling techniques. Atmospheric Environ., 79, 716-730
- Torres P, Le Clainche S, Vinuesa R (2021) On the Experimental, Numerical and Data-Driven Methods to
- 1120 Study Urban Flows. Energies, 14, 1310
- 1121 United Nations Department of Economic and Social Affairs (2018) 68% of the world population projected
- 1122 to live in urban areas by 2050, says UN. Available
- online: https://www.un.org/development/desa/en/news/population/2018-revision-of-world-
- 1124 urbanization-prospects.html.
- Wallace JM (2016) Quadrant analysis in turbulence research: History and evolution, Ann. Rev. Fluid Mech.,
- 1126 48:131-158
- Wang L, Li D, Gao Z, Sun T, Guo X, Bou-Zeid E (2014) Turbulent transport of momentum and scalars above
- an urban canopy. Boundary-Layer Meteorol. 150(3):485–511
- Wang Y, Vita G, Fraga B, Wang J, Hemida H (2021) Effect of the Inlet Boundary Conditions on the Flow
- over Complex Terrain Using Large Eddy Simulation. Designs, 5(2), 34
- 1131 Wilson NR, Shaw RH (1977) A higher order closure model for canopy flow. J. Appl.
- 1132 Meteorol. 16 (11), 1197–1205
- 1133 Wu X (2017) Inflow turbulence generation methods. Ann. Rev. Fluid Mech., 49, 23-49
- 1134 Xie ZT, Castro IP (2006) LES and RANS for Turbulent Flow over Arrays of Wall-Mounted Obstacles. Flow
- 1135 Turbul. Combust. 76, 291
- 1136 Xie ZT, Coceal O, Castro IP (2008) Large-eddy simulation of flows over random urban-like obstacles.
- Boundary-Layer Meteorol 129:1–23
- 1138 Xie ZT, Castro IP (2009) Large-eddy simulation for flow and dispersion in urban streets, Atmospheric
- 1139 Environ, 43, 2174-2185

1140	Xie ZT, Fuka V (2018) A Note on Spatial Averaging and Shear Stresses Within Urban Canopies. Boundary-
1141	Layer Meteorol 167, 171-179
1142 1143	Yuan J, Piomelli U (2014) Roughness effects on the Reynolds stress budgets in near-wall turbulence. J. Fluid Mech. 760: R1–R12
1144	Zhou Y, Li D, Liu H, Li X (2018) Diurnal Variations of the Flux Imbalance Over Homogeneous and
1145	Heterogeneous Landscapes. Boundary-Layer Meteorol 168, 417–442